



저작자표시-비영리-변경금지 2.0 대한민국

이용자는 아래의 조건을 따르는 경우에 한하여 자유롭게

- 이 저작물을 복제, 배포, 전송, 전시, 공연 및 방송할 수 있습니다.

다음과 같은 조건을 따라야 합니다:



저작자표시. 귀하는 원저작자를 표시하여야 합니다.



비영리. 귀하는 이 저작물을 영리 목적으로 이용할 수 없습니다.



변경금지. 귀하는 이 저작물을 개작, 변형 또는 가공할 수 없습니다.

- 귀하는, 이 저작물의 재이용이나 배포의 경우, 이 저작물에 적용된 이용허락조건을 명확하게 나타내어야 합니다.
- 저작권자로부터 별도의 허가를 받으면 이러한 조건들은 적용되지 않습니다.

저작권법에 따른 이용자의 권리는 위의 내용에 의하여 영향을 받지 않습니다.

이것은 [이용허락규약\(Legal Code\)](#)을 이해하기 쉽게 요약한 것입니다.

[Disclaimer](#)

Master's Thesis
석사학위논문

The Synthesis and Characterization of Colloidal Nanocrystals for Perovskite Solar Cells

Seung-Ho Lee(이 승 호 李 勝 鎬)

Department of Energy Systems Engineering
에너지시스템전공

DGIST

2016

Master's Thesis
석사학위논문

The Synthesis and Characterization of Colloidal Nanocrystals for Perovskite Solar Cells

Seung-Ho Lee(이 승 호 李 勝 鎬)

Department of Energy Systems Engineering
에너지시스템전공

DGIST

2016

The Synthesis and Characterization of Colloidal Nanocrystals for Perovskite Solar Cells

Advisor : Professor Jong-Soo Lee

Co-advisor : Professor Nak Cheon Jeong

by

Seung-Ho Lee

Department of Energy Systems Engineering

DGIST

A thesis submitted to the faculty of DGIST in partial fulfillment of the requirements for the degree of Master of Science in the Department of Energy System Engineering. The study was conducted in accordance with Code of Research Ethics¹

05. 30. 2016

Approved by

Professor Jong-Soo Lee(Signature)
(Advisor)

Professor Nak Cheon Jeong(Signature)
(Co-Advisor)

¹ Declaration of Ethical Conduct in Research: I, as a graduate student of DGIST, hereby declare that I have not committed any acts that may damage the credibility of my research. These include, but are not limited to: falsification, thesis written by someone else, distortion of research findings or plagiarism. I affirm that my thesis contains honest conclusions based on my own careful research under the guidance of my thesis advisor.

The Synthesis and Characterization of Colloidal Nanocrystals for Perovskite Solar Cells

Seung-Ho Lee

Accepted in partial fulfillment of the requirements for the degree of Master of
Science.

05. 30. 2016

Head of Committee _____(인)

Prof. Jong-Soo Lee

Committee Member _____(인)

Prof. Nak Cheon Jeong

Committee Member _____(인)

Prof. Youn-Gu Lee

MS/ES
201424013

이 승 호. Seung-Ho Lee Colloidal Quantum Dots as Hole-transporting Materials for Hybrid Perovskite Solar Cells 2016. 40p. Advisor Prof. Jong-Soo Lee. Co-Advisor Prof. Nak Cheon Jeong.

ABSTRACT

In recent times, the emergence of organic-inorganic halide perovskite materials have been considerable attention to many scientists in photovoltaic fields due to high light absorption coefficient, outstanding charge carriers diffusion length and optical band gap as light absorbers.

Herein, we have applied colloidal quantum dots to hole-conducting layers in methylammonium lead triiodide-based perovskite solar cells. First, we use lead sulfide(PbS), colloidal quantum dots(QDs) which are synthesized by hot-injection method due to low-cost, solution-processable materials, strong absorption coefficient and size-dependent optical properties compared to expensive organic-conducting materials. They are spin-coated on mesoscopic perovskite layers to form n-i-p junctions. The devices with different optical band gaps of PbS QDs show slightly enhanced current density contrary to reduced open-circuit voltages than hole-free perovskite solar cells. The maximum power conversion efficiency has reached 6.7% with PbS QDs. We also synthesized Au-PbS core-shell structures for the hole-transporting layer due to strong p-type doping effect resulting in enhanced hole transfer and the relation between plasmon from cores and excitons from shells. Furthermore, we have applied CZTS and CZTSe QDs composed of quaternary Copper-Zinc-Tin-Sulfur or Selenium compounds to hole transport layer for enhancing the photovoltaic performances and tuning band gaps of perovskite solar cells. CZTS and CZTSe QDs with diameters of 10 to 20nm were

also synthesized by hot-injection method and when they are spin-coated on the absorber layer solar cell devices show higher current density, open-circuit voltage and IPCE than hole-conducting materials free perovskite solar cell. Their maximum power conversion efficiency has been over 7% and open-circuit voltage has been changed depending on particle's compositions.

Keywords: hot-injection method, Perovskite solar cells, n-i-p heterojunction solar cell, colloidal quantum dots, PbS, CZTS QDs, CZTSe QDs

Contents

Abstract	i
List of contents	iii
List of figures	v
List of tables	vi
1. Introduction	1
2. Theoretical Section	4
2.1. Colloidal Quantum Dots	4
2.1.1. Solution phase synthesis of quantum dot nanoparticles	4
2.1.2. Properties of colloidal quantum dot nanoparticles	4
2.2. Perovskite Solar Cells	5
2.2.1 The advancement of efficiency in perovskite solar cells	5
2.2.2 Properties of organic-inorganic perovskite materials	6
2.2.3 Structural types of perovskite solar cells	7
2.2.4 Fabricating solution-processed perovskite solar cells	8
3. Experimental Section	9
3.1. Materials	9
3.2. Synthesis of Colloidal Quantum Dots	9
3.2.1. Synthesis of colloidal gold nanocrystals	9
3.2.1. Synthesis of colloidal PbS quantum dots	10
3.2.2. Synthesis of colloidal Au-PbS quantum dots	10
3.2.3. Synthesis of colloidal $\text{Cu}_2\text{ZnSnS}_4$ quantum dots	11
3.2.4. Synthesis of colloidal $\text{Cu}_2\text{ZnSnSe}_4$ quantum dots	12
3.3. Solar Cell Fabrication	12
3.4. Characterization	14
4. Results & Discussion	16

4.1. Characterization of colloidal quantum dots	16
4.2. Characterization of Perovskite films.....	22
4.3. Characterization of Perovskite solar cells with nanocrystals	27
5. Summary & conclusion	35
6. References	36

List of Figures

Figure 2.1 Schematic image of hot-injection method of colloidal synthesis

Figure 2.2 Latest efficiencies of photovoltaic devices. Reprinted from NREL

Figure 2.3 A lattice structure of perovskite materials. ABX_3

Figure 2.4 n-i-p structure of perovskite solar cells. (a) mesoscopic concept with TiO_2 nanoparticles, (b) planar heterojunction type

Figure 2.5 Two kinds of fabrication solution-processable perovskite solar cells

Figure 4.1.1. TEM images of (a) Au NPs, (b) PbS QDs, (c) Au-PbS core-shell NCs. (d) HR-TEM image of Au-PbS core-shell NCs

Figure 4.1.2. XRD patterns of PbS QDs coated on the glass substrates

Figure 4.1.3 UV-vis-NIR spectra of (a) Au NCs, (b) PbS QDs with different first exciton absorption peaks and (c) Au-PbS core-shell NCs

Figure 4.1.4. XRD patterns for as-synthesized $Cu_2ZnSnSe_4$ and Cu_2ZnSnS_4 nanocrystals on the glass substrates.

Figure 4.1.5. TEM images of (a) Cu_2ZnSnS_4 and (b) $Cu_2ZnSnSe_4$ quantum dots

Figure 4.1.6. (a) UPS spectrum of as-deposited CZTS and CZTSe NCs on the glass substrate, (left) the valence band edge in the short-range binding energy, (right) general UPS spectrum. (b) $(\alpha h\nu)^2$ vs energy plots where CZTS and CZTSe NCs are determined to be 2.2eV and 1.92eV respectively

Figure 4.2.1. Top view SEM images of (a) mesoporous TiO_2 (30nm) films, (b) PbI_2 films on mesoporous TiO_2 layer and (c) $CH_3NH_3PbI_3$ perovskite films with 10mg/ml MAI solution

Figure 4.2.2. XRD patterns of PbI_2 and $CH_3NH_3PbI_3$ films on the glass substrates

Figure 4.2.3. Top view SEM images of the perovskite film with different heat treatments on the preheated mesoscopic layer. (a) room temperature (b) 50 °C (c) 70 °C glass coated on TiO_2

Figure 4.2.4 (a) Schematic structure of the device. (b) Cross-sectional SEM image of TiO_2 / $CH_3NH_3PbI_3$ / Spiro-

OMeTAD / Au

Figure 4.2.5. (a) Current density-Voltage curve of CH₃NH₃PbI₃ device with spiro-OMeTAD under AM 1.5G spectrum (100mWcm⁻²) in the air (b) IPCE spectrum of the device with spiro-OMeTAD in the air

Figure 4.3.1. Energy level diagram of TiO₂ / CH₃NH₃PbI₃ / PbS QDs / Au

Figure 4.3.2. Top view SEM image of (a) PbS-coated perovskite films. Cross-sectional SEM image of TiO₂ / CH₃NH₃PbI₃ / PbS QDs / Au

Figure 4.3.3. Current density-Voltage curve of CH₃NH₃PbI₃ device with different sizes of PbS QDs under AM 1.5G spectrum (100mWcm⁻²) in the air (b) IPCE spectrum of the device with different sized PbS QDs

Figure 4.3.4. Energy level alignment for CZTS and CZTSe QDs based perovskite solar cell

Figure 4.3.5 Top-view (a, c) and cross-sectional (b, d) scanning electron microscopy (SEM) images of the devices based on MAPbI₃ perovskite layers by two-step deposition method. CZTS quantum dots coated on the perovskite layer (a, b) and CZTSe quantum dots coated on the perovskite layer (b, d).

Figure 4.3.6. UV-Vis-NIR absorption spectra for different types of films. TiO₂ / CH₃NH₃PbI₃, TiO₂ / CH₃NH₃PbI₃ / CZTS QDs and TiO₂ / CH₃NH₃PbI₃ / CZTSe QDs. (b) Normalized time-resolved photoluminescence decay aspects of perovskite films with different hole-conducting materials.

Figure 4.3.7. (a) Current-Voltage curves of CH₃NH₃PbI₃ devices with different hole-transporting layers measured under AM 1.5G illumination (100mW cm⁻²) in the air. (b) External quantum efficiency spectra of solar cells measured in the air

List of Tables

Table 4.1. Valence and conduction band edge of CZTS and CZTSe QDs

Table 4.2. Photovoltaic parameters for the perovskite solar cell with Spiro-OMeTAD

Table 4.3. Photovoltaic parameters for the perovskite solar cell with different sized PbS QDs

Table 4.4. Photovoltaic parameters for the perovskite solar cell with CZTS and CZTSe QDs

1. Introduction

Due to rapidly growing world population, energy consumption with burning fossil fuels have been also increasing every year. Excessive CO₂ gases that are come from fossil fuels bring about global warming, causing unexpected climate such as El Nino, heat wave and such. To solve the problems, the light of sun in the renewable energy has been attention to many scientists because of an infinite energy source and zero carbon energy for generating electricity. Above all, solar cells have been regarded as a promising means directly converting the light into electricity. Commonly used solar cells are based on crystalline silicon materials but they have problems that silicon materials absorb too narrow wavelengths to limit performance of solar cells and the cost of production is high. Thus, new types of solar cells has emerged to complement those defects. One of the famous things in a variety of solar cells is perovskite-based solar cells. Perovskite materials, CH₃NH₃PbBr₃ and CH₃NH₃PbI₃, were first introduced in dye-sensitized solar cells (DSSCs) by T. Miyasaka and co-workers in 2009¹. They reported CH₃NH₃PbI₃ and larger-band gap CH₃NH₃PbBr₃ could be used as absorbers and sensitizers in liquid-electrolyte-based DSSCs, the highest power conversion efficiency (PCE) reached 3.8% when CH₃NH₃PbI₃ and iodide-based electrolyte were employed but the stability was poor due to the reaction between sensitizers and liquid electrolyte. Since then, N.G Park and co-workers have improved the performance of perovskite-based DSSCs by changing electrolyte, TiO₂ process and processing of depositing perovskite nanocrystals, resulting in higher PCE of 6.5% and enhanced stability compared with the previous thing². However liquid-electrolyte-based perovskite solar cells were still degraded in the short time due to liquid solution. When N. G. Park in collaboration with the group of M. Grätzel suggested a solid-state hole-transporting

material to replace the liquid electrolyte, it has made perovskite solar cells advanced in terms of the stability and performance of cells³. Since solid-state hole-transporting materials were applied to perovskite solar cells, many groups researching perovskite solar cells in the world have reported extremely high performance of the solar cells in many different compositions and different processes^{4,5}. To date, the certified power conversion efficiencies have risen to more than 20% in just 3 years⁶ and most of those groups have commonly used state-of-the-art HTM such as PTAA, spiro-MeOTAD (2,2',7,7'-tetrakis- (N,N-di-p-methoxyphenylamine)-9,9'-spirobifluorene)), P3HT, in n-i-p heterojunction perovskite solar cells.⁷ However, it is difficult for commonly used polymers to be commercialized to the photovoltaic markets because of complicated synthetic processes for high-quality powders which result in production cost rise and poor hole-mobility without p-dopants.⁸ In terms of them, inorganic hole-transporting materials which have cheaper price concerning easily synthetic routes, high hole mobility and higher stability than organic materials have been suitable replacement materials in perovskite solar cells based on organic-composed HTMs.⁹ Inorganic HTMs have been already reported by a few groups.^{10,11,12} Among inorganic HTMs, colloidal quantum dots have been good candidates that they have low-band-gap to be tuned properly to the band gaps of perovskite materials by simple methods and additional ability to harvest near-infrared region, causing much higher photocurrent density^{13,14,15} with compensating the absorption of the perovskite layers. Furthermore, colloidal quantum dots as hole-transporting or electron-transporting materials have reached more than 10%.^{16,17,18} Although quantum dot based perovskite solar cells have many challenges to enhance properties of perovskite solar cells like capping organic ligands and interface between layers, they could be potential to enhance photovoltaic parameters.

In this report, we synthesized and characterized colloidal nanoparticles. Among them, we

report well-known p-type colloidal quantum dots such as PbS, Au-PbS, Cu₂ZnSnS₄ (CZTS), Cu₂ZnSnSe₄ (CZTSe) QDs and applied to hole-transporting layers in perovskite solar cells. PbS quantum dots have been already reported as absorbers for photovoltaic devices^{19,20,21} due to high absorption coefficient and a wide range of tunable band gaps. Surely, PbS quantum dots have been investigated to replace organic-conducting polymers with them.²² We have introduced solution-processed PbS QDs as a hole-transporting material for mesoscopic perovskite solar cells. When the different sizes of PbS QDs, characterized by optical measurements, were applied they did show higher current density and slightly changed open-circuit voltages through measurements. When the Au-PbS core-shell nanostructures were applied to the hole-transporting layer, it couldn't show higher performance than expected. We have also investigated the effect of open-circuit voltage in perovskite solar cells as CZTS and CZTSe QDs were applied to hole-conducting layers. Properties of CZTS and CZTSe quantum dots have been reported by synthetic groups and device groups.^{23,24} The results of optical measurements and photovoltaic measurements showed different stoichiometry of quantum dots had an effect on V_{oc} of the devices and efficient hole transporter.

2. Theoretical Section

2.1 Colloidal Quantum Dots

2.1.1 Solution phase synthesis of quantum dot nanoparticles

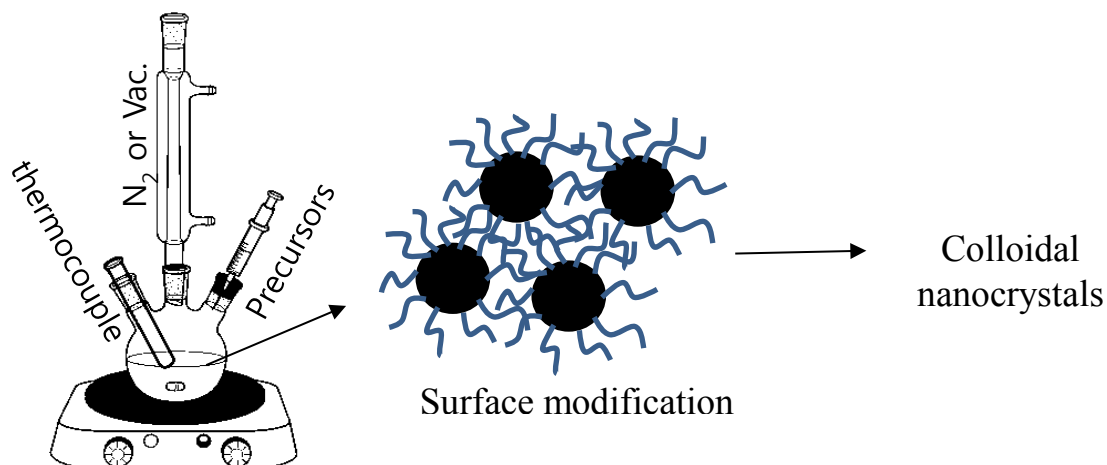


Figure 2.1 A schematic image of hot-injection method of colloidal synthesis.

Colloidal synthesis using semiconducting materials and organic solvents has been one of the most powerful methods in the production of nanocrystals. This method was first introduced by Brus and Henglein in 1908. Time passed, high-quality and monodisperse colloidal quantum dots (CQD) were presented by Murray et al.²⁵ When injecting the precursors into the reaction flask, atomic species constitute certain sizes of the nanocrystals with the deposition of organic capping groups like OA, TOP, TOPO and so on. Organic solvents serve two goals. Its main goal is enhancing the solubilization of metallic compounds and dispersing nanocrystals and the reactants in the growth mechanism. Another goal is controlling the reaction rate. The growth of nanocrystals is influenced by the attachment or detachment of solvent molecules, called surface ligands or surfactants. The surfactant molecules have non-polar alkyl chains and polar head groups. The form of the non-polar group and the binding strength of the polar group in organic

solvents affects the growth mechanisms of nanocrystals.²⁶ Based on these points, Solution-based nanocrystal synthesis is easily controllable size and the shape of nanocrystals with low cost productions²⁷ and can be applied to many electronic devices.²⁸

2.2.2 Properties of colloidal quantum dot nanoparticles

Colloidal quantum dots are nanometer-sized semiconducting materials. Among their properties, quantum confinement effect is a representative property which correlate band gap tunability and occur when the length scales of atomic structures reach 1 to 25nm in IV, III-V, II-VI semiconducting materials and electronic wave function is similar to particle size. It also happens that the dimensions of semiconductor particles (quantum dots) are less than bohr exciton radius. With this in effect, continuous energy band levels are changed to be discrete like atomic band levels. Discrete band levels or states has each absorption spectrum.

2.2 Perovskite Solar Cells

2.2.1 The advancement of efficiency in perovskite solar cell

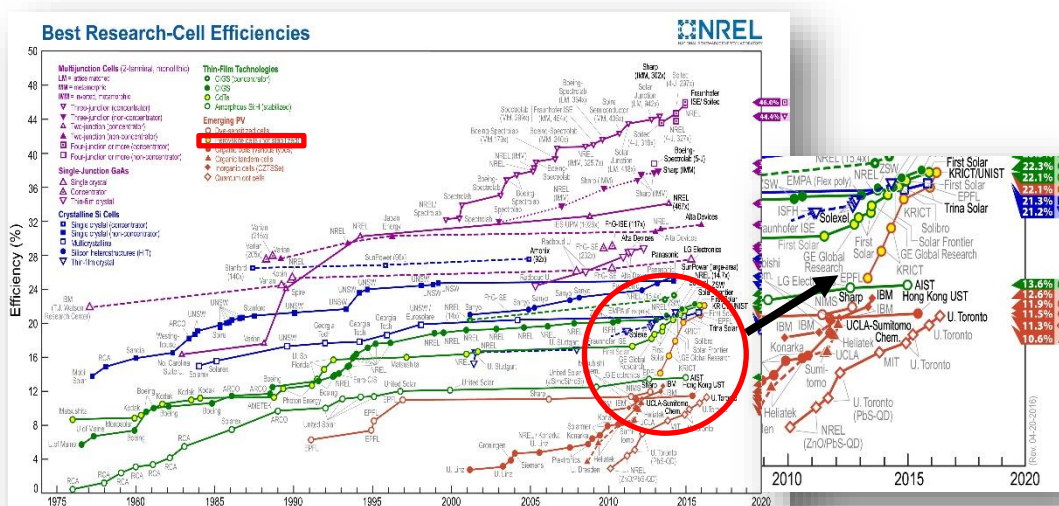


Figure 2.2 Latest efficiencies of photovoltaic devices. Reprinted from NREL.

Since perovskite materials were applied to DSSCs as a sensitizer and collaborated with solid-state hole-transporting materials, solid-state perovskite solar cells have been dramatically attention to engineers in the world compared with other types of solar cells.²⁹ Recently, the efficiency of perovskite solar cells reached more than 21% by EPFL⁶ and KRIC/UNIST groups through more advanced fabrications and it will have been continuous issues in photovoltaic fields.

2.2.2 Properties of organic-inorganic perovskite materials

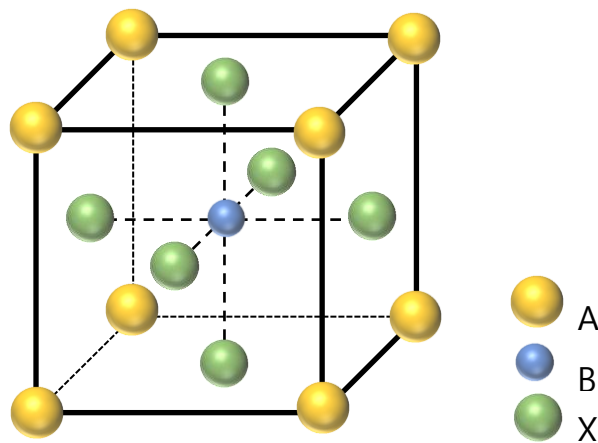


Figure 2.3 A lattice structure of perovskite materials. ABX_3

The stoichiometry of perovskite materials is ABX_3 with cubic crystal structure. A is an organic cation (generally $CH_3NH_3^+$ or $(NH_2)_2CH^+$ or inorganic components like Cs^+), located at cubooctahedral sites, B is a metal cation (generally Pb^{2+} etc), and X is a halide anions (I^- , Br^- or Cl^-). The indicator for stability and distortion of perovskite materials is tolerance factor (t), $t = (R_A + R_B) / [\sqrt{2}(R_B + R_X)]$, where R_A, R_B and R_X are ionic radius for A, B and X ions each.³⁰ As t value approaches 1, it means ideal cubic perovskite. Based on $CH_3NH_3PbI_3$, the absorption coefficient (α), which determines how far into a material light of a particular wavelength can penetrate before it is absorbed, was measured to be $1.5 \times 10^4 \text{ cm}^{-1}$ at 550nm, indicating

penetration depth $0.66\mu\text{m}$, and $0.5 \times 10^4\text{cm}^{-1}$, indicating penetration depth $2\mu\text{m}$, which means it is suitable for absorbers in photovoltaic devices. The valence, conduction band level and band gap of $\text{CH}_3\text{NH}_3\text{PbI}_3$, typically used, was reported to be -5.43eV , -3.93eV and 1.5eV through optical measurement.³

2.2.3 Structural types of perovskite solar cells

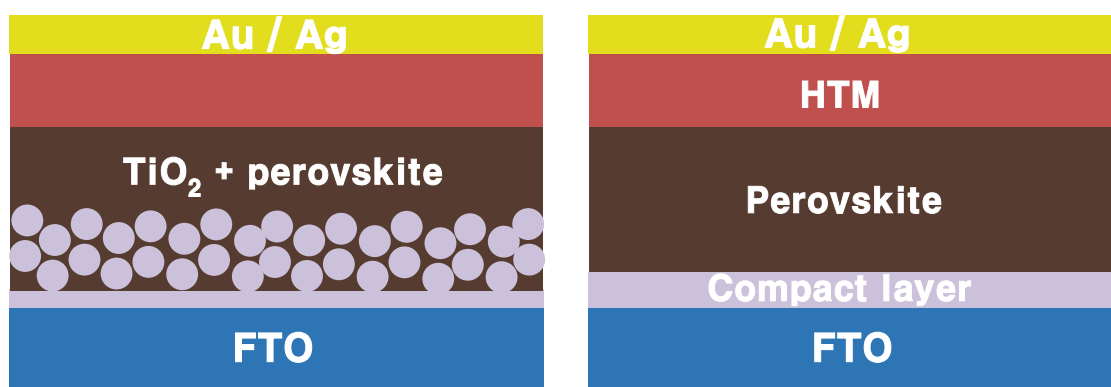


Figure 2.4 n-i-p structure of perovskite solar cells. (a) mesoscopic concept with nanooxide materials, (b) planar heterojunction type

There are two types of n-i-p perovskite solar cells as commonly fabricated. The n-i-p structure consists of n-type semiconductors (electron-transporting materials) contacting on transparent conducting substrates and intrinsic semiconductors and p-type semiconductors hole-transporting materials) contacting on electrodes. Porous TiO_2 and Al_2O_3 ³¹ have been commonly used as n-type materials and $\text{CH}_3\text{NH}_3\text{PbX}_3$ ³² or FAPbX_3 ³³ or CsPbX_3 ^{34,35} have been commonly used as absorber layers and Spiro-MeOTAD^{8,36} or PTAA⁵ have been in common use as p-type materials. In early steps, perovskite solar cells containing porous TiO_2 and Al_2O_3 did lead to highly efficient solar cells but there were some problems concerning hysteresis.^{37,38} Planar heterojunction types or many kinds of perovskite solar cells have appeared to solve that

problem.³⁹

2.2.4 Fabricating solution-processed perovskite solar cells

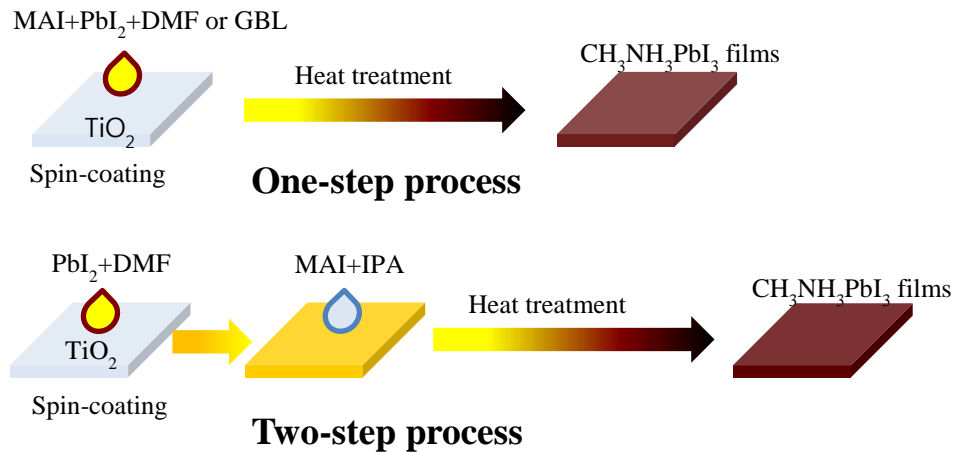


Figure 2.5 Two kinds of fabrication solution-processable perovskite solar cells

There are two fabrication processes in solution-processed perovskite solar cells. One-step process is that CH₃NH₃PbI₃ and PbI₂ powders are dissolved in DMF or r-butyloractone² and the solution is coated on pre-treated glasses. That had a problem concerning the uniformity.⁴⁰ After solvent engineering or other techniques appeared^{41,42,43}, large grain-sized perovskite films have been achieved to be highly efficient solar cells. Two-step process is also used to fabricate devices. This is slightly different from one-step process. PbI₂ powders are dissolved in DMF and the solution is coated on pretreated glasses and then a certain concentration of CH₃NH₃I dissolved is loaded on PbI₂ coated glasses. As reported by N.G park et al⁴⁴, the concentration of CH₃NH₃I solutions affected growth of perovskite films or morphologies.

3. Experimental Section

3.1 Materials

Gold(III) chloride(99.99%, Alfa), didodecyldimethyl ammonium bromide(DDAB, 98%, Aldrich), Sodium borohydride(NaBH_4 , 99%, Aldrich), tetrabutyl ammonium borohydride(TBAB, 98%, Aldrich), 1-dodecanethiol(1-DDT, $\geq 98\%$, Aldrich), lead(II) oxide (99.999%, Aldrich), 1-octadecene (ODE, 90%, Aldrich), oleic acid (OA, 90%, Aldrich), hexamethyldisilthiane (TMS_2S , Aldrich), platinum(IV) chloride(99.99%, Alfa), Copper(II) acetylacetonate ($\text{Cu}(\text{acac})_2$, 99.99%, Aldrich), tin(IV) acetate ($\text{Sn}(\text{OAc})_4$, Aldrich), zinc acetate ($\text{Zn}(\text{OAc})_2$, 99.99%, Aldrich), sulfur powder (S, 99.98%, Aldrich), selenium powder (Se, 99.99%, Aldrich), trioctylphosphine oxide (TOPO, 99%, Aldrich)

3.2 Synthesis of Colloidal Quantum Dots

3.2.1 Synthesis of colloidal gold nanoparticles

We modified the synthesis of gold nanoparticles reported by Prasad et al.⁴⁵ In a typical procedure, 0.068g gold(III) chloride and 0.185g DDAB(didodecyldimethylammonium bromide) were dissolved into 20mL toluene by sonication for 1h. After fully dissolved(red color solution), we prepared a solution composed of 0.07g NaBH_4 and 0.2mL deionized water and dropped slowly into the solution with vigorous stirring for reduction reaction of gold ions. The color of the solution were changed from red to purple during the reaction. After 30 minutes, 1.6mL 1-didodecanethiol was added to the solution and the solution were kept stirring for 5 minutes. To extract final products from the crude solution, Ehtanol was added to the solution, which was consecutively precipitated by centrifugation. Purple precipitates were dispersed in a suitable amount of toluene and then filtered by 0.45 micron filter. All experiments were

carried out in ambient condition.

3.2.2 Synthesis of colloidal PbS quantum dots

The synthesis of PbS quantum dots was followed to the previous method reported by J.S Lee et al⁴⁶. 0.226g of lead oxide, 5ml ODE and 5ml OA were prepared in a 25mL 3-neck round-bottom flask and stirred quickly and heated to 140 °C for 1 h under the vacuum condition to make lead oleate precursors. The mixture of 120µl TMS₂S and 2ml dry ODE were prepared in the glove box. After cooling to 100 °C, TMS₂S-ODE solution was injected into the flask and quickly quenched to room temperature using ice-water bath to make proper sizes of quantum dots. After then, the quantum dots were separated from product solution. To precipitate quantum dots, we added ethanol/hexane solution to product solution by centrifugation. This step was carried out several times to get mono-disperse particles. Final products were re-dispersed into hexane or non-polar solvents. They were keep in a nitrogen-filled glove box. The particles have different sizes with different temperature and duration time.

3.2.1 Synthesis of colloidal Au-PbS quantum dots

We consulted the synthesis method reported by J.S Lee et al.⁴⁶ All experiments were carried out by using Schlenk line connected to nitrogen and vacuum line to prevent oxidation and moisture. 0.226g lead oxide were put into 5mL ODE and 5mL OA. The solution was stirred intensively and heated to 140 °C for 1h under vacuum condition. After that, the mixture was cooled to 100 °C slowly and kept it at 100 °C for 5minutes under nitrogen condition. Prepared Au nanoparticles(about 4nm, 1.2mL solution) were then injected to the precursor and kept it at 100 °C for 5minutes to evaporate toluene from the mixture. The solution was heated to 120 °C

and then the mixture of 120 μ l TMS₂S and 2ml dry ODE was injected. After reaction, the color of solution were changed to dark-brown and kept at 120°C for 7 minutes to grow PbS shells. The solution was quenched to room temperature by a water bath in 7 minutes and precipitate the product, using ethanol and hexane. To get monodisperse core-shell structure, washing procedure was carried out three times. The final product was dispersed in hexane or chlorobenzene.

3.2.2 Synthesis of colloidal Cu₂ZnSnS₄ quantum dots

We followed synthesis procedures reported by Amy L. Prieto et al.²⁴ In a typical procedure, 0.4585g Cu(acac)₂, 0.1975g Zn(OAc)₂, 0.3325g Sn(OAc)₂ and 15mL OLA were prepared in a 25mL 3-neck round-bottom reaction flask and stirred vigorously and heated to 150°C under vacuum condition. The temperature was cooled to 125°C and the precursor was kept at 125°C until injection. The mixture 0.212g Sulfur powders and 0.151g NaBH₄ and 15mL OLA was sonicated in a 20mL until fully dissolved, approximately 1h. 50mmol TOPO in a 50mL 3-neck round-bottom flask was heated to 325°C under vacuum condition and nitrogen atmosphere.

Sulfur-based and Cu-Zn-Sn-based precursors had been ready to inject to a 50mL 3-neck round-bottom flask rapidly via glass syringe for metal precursors and luer-lock tip syringe for Sulfur precursors before reaching temperature was 325°C. At 325°C, prepared precursors were injected to a 50mL flask at the same time. When the temperature was lowered to 285°C, after 5minutes, the mixture was quenched to room temperature by air-cooled method. To obtain final products, methanol was added to the product for removing residues like organic ligands. CZTS quantum dots were washed three times for mono-disperse and uniform nanoparticles. The product was redispersed in chlorobenzene or non-polar solvents.

3.2.3 Synthesis of colloidal $\text{Cu}_2\text{ZnSnSe}_4$ quantum dots

We followed synthesis procedures as above. Procedures were almost same but different, especially changing sulfur powder into selenium powder. In a typical procedure, 0.4585g $\text{Cu}(\text{acac})_2$, 0.1975g $\text{Zn}(\text{OAc})_2$, 0.3325g $\text{Sn}(\text{OAc})_2$ and 15mL OLA were prepared in a 25mL 3-neck round-bottom reaction flask and stirred vigorously and heated to 150°C under vacuum condition. The temperature was cooled to 125°C and the precursor was kept at 125°C until injection. The mixture 0.521g Selenium powders and 0.151g NaBH_4 and 15mL OLA was sonicated in a 20mL until fully dissolved, approximately 1h. 50mmol TOPO in a 50mL 3-neck round-bottom flask was heated to 325°C under vacuum condition and nitrogen atmosphere.

Sulfur-based and Cu-Zn-Sn-based precursors had been ready to inject to a 50mL 3-neck round-bottom flask rapidly via glass syringe for metal precursors and luer-lock tip syringe for Sulfur precursors before reaching temperature was 325°C. At 325°C, prepared precursors were injected to a 50mL flask at the same time. When the temperature was lowered to 285°C, after 5minutes, the mixture was quenched to room temperature by air-cooled method. To obtain final products, methanol was added to the product for removing residues like organic ligands. CZTS quantum dots were washed three times for mono-disperse and uniform nanoparticles. The product was re-dispersed in chlorobenzene or non-polar solvents

3.3 Solar Cell Fabrication

The photovoltaic devices were fabricated on the fluorine-doped tin oxide-coated glasses(around $\sim 13\Omega/\text{sq}$, Pilkington). The patterned glasses were prepared by etching specific areas through reactions between zinc powder(extra pure, duksan) and hydrochloric acid(20%,

daejung). After patterning the FTO glasses, they were rinsed with deionized water, detergent, acetone, ethyl alcohol and dried using nitrogen gas-blowing and subsequently treated by oxygen plasma for 20minutes.

The compact layers of TiO₂ (~30nm thickness) were deposited on the substrates by aerosol spray pyrolysis method at 500°C using a solution containing 0.3ml titanium diisopropoxide bis(acetylacetonate) solution(75% in 2-propanol, Aldrich) diluted in 4mL ethanol(99.9%, Fisher) under ambient condition. After cooling down to room temperature, the substrates were cut in the shape of squarthen e, 1.5cm x 1.5cm.

The mesoporous layers composed of a TiO₂ paste (Dyesol 30NRD, Dyesol) diluted in ethanol(1:3.5, weight ratio) were deposited on compact layer by spin-coating at 5000rpm for 30s³⁶ and then dried at 125°C for 5 minutes. After that, the films were heated at 500°C for 1h. When the temperature reached to room temperature, the films were immersed into 0.2M TiCl₄ aqueous solution(Aldrich) and rinsed with deionized water and subsequently heated at 500°C for 1h. The thickness of mesoporous TiO₂ layers was about 400nm.

The deposition of perovskite layers was followed to N.G park et al⁴⁰, two-step deposition. 461mg PbI₂ powder(99%, Aldrich) was fully dissolved in 1ml DMF(≥99%, anhydrous, Aldrich) at 70°C for 30 minutes and then filtered with 0.45μm pore-size hydrophilic syringe filters. The solution was kept and stirred at 70°C during whole process. 30μl PbI₂ solution was spin-coated at 3000rpm for 20s on the pre-heated substrates and then heated at 40°C 3min, 100°C 5 min subsequently. After cooling down to room temperature, PbI₂-coated films were

dipped in a solution of $\text{CH}_3\text{NH}_3\text{I}_3$ in 2-propanol(10mg/ml, 0.063M) for 30s and rinsed with 2-propanol followed by spin-coating at 4000rpm for 12s. After that, 100 μL of 0.063M $\text{CH}_3\text{NH}_3\text{I}_3$ solution in 2-propanol(anhydrous, Aldrich) was loaded on the substrates for 20s, which was spun at 4000rpm for 20s and then dried at 100 $^\circ\text{C}$ for 10min.

The HTM (~30 μL) was spin-coated on the perovskite layers at 4000rpm for 30s, which was prepared by dissolving 28.9mg 2,2',7,7'-Tetrakis(N,N-di-p-methoxyphenylamino)-9,9'-spirobifluorene (spiro-MeOTAD, $\geq 99.5\%$, Luminescence Technology corp.), 16.5 μL 4-tert-butylpyridine(96%, Aldrich), 7 μL of lithium bis(trifluoromethanesulfonyl)amide (Li-TFSi, Aldrich) solution (520mg Li-TFSi in 1ml acetonitrile(99.8%, Aldrich)) and 8.8 μL of cobalt(III) complex FK209 TFSI salt (Dyesol) in 400 μL chlorobenzene(99.8%, Aldrich). The inorganic HTMs, colloidal PbS QDs or Au-PbS core-shells or CZTS QDs or CZTSe QDs capped with organic ligands and dispersed in non-polar solvents as chlorobenzene or octane, were spin-coated on the perovskite layers at 4000rpm for 30s.

Finally, 100nm thickness of gold was deposited by thermal evaporator under high vacuum condition ($<10^{-5}$ Torr) on the top of the devices as back contacts. All fabrication of the perovskite devices were carried out under ambient condition.

3.4 Characterization

Transmission electron microscopy (TEM) The morphologies of nanoparticles were characterized using a Hitachi HF-3300 FE-TEM operating an accelerating 300kV. The samples were prepared on the carbon-coated copper grids(Ted Pella).

Scanning electron microscopy (SEM) Nanostructured materials were characterized using S-4800 Hitachi FE-SEM (3kV) or SU-8020 Hitachi HR FE-SEM (3kV). Samples were prepared on FTO glass substrates by spin-coating and putting carbon paste electrode.

Powder X-ray diffraction (XRD) XRD patterns of were collected using a Rigaku MiniFlex 600 equipped with monochromatic Cu K α radiation source at 298K. The nanoparticles on the glass were prepared by drop casting and then dried at 70°C to evaporate organic solvents in ambient condition(PbS) or N₂-filled glovebox.(CZTS, CZTSe)

Time-resolved photoluminescence (TRPL) Time resolved photoluminescence decays of perovskite films were carried out using a time-correlated single-photon counting system utilizing Picoquant Model PicoHarp 300, a picosecond pulsed diode laser driver using Picoquant Model PDL 800-D with laser head LDH P-C-375 operating at 375 nm wavelength. The decays were generated at 770nm and fitted with double exponential decay.

Ultraviolet photoelectron spectroscopy (UPS) The UPS spectra of CZTS and CZTSe QDs were carried out to certify band alignment of them in an ultraspectrometer (ESCALAB 250Xi, Thermo Scientific) equipped with He I (21.2 eV) discharge lamp.

Optical measurement Absorption spectra were collected using Agilent Cary 5000 UV-vis-NIR spectrophotometer. Spectroscopic analysis was carried out in solution for nanocrystals and in solid-state films for perovskite solar cells

Photovoltaic measurement Photocurrent density-voltage (J-V) was characterized with a solar simulator (K-3300, McScience) giving light intensity AM 1.5G (100mW/cm²), calibrated by a c-Si photodiode (K801S-K13, McScience) as a reference. The active area of the square cells is 0.05cm². The incident photon conversion efficiency (IPCE) spectra was measured using an IPCE measurement system (K3100, McScience)

4. Results & Discussion

4.1 Characterization of colloidal quantum dots

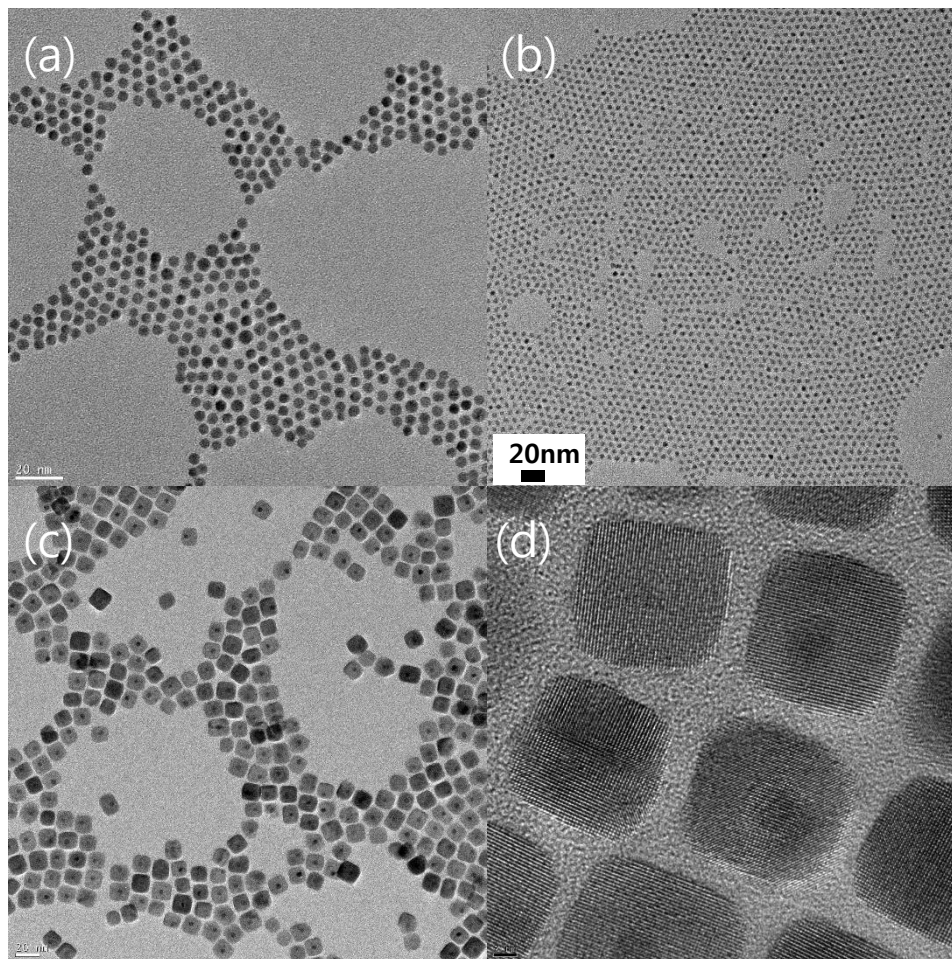


Figure 4.1.1. TEM images of (a) Au NPs, (b) PbS QDs, (c) Au-PbS core-shell NCs. (d) HR-TEM image of Au-PbS core-shell NCs.

We synthesized gold nanocrystals capped with organic ligands like 1-DDT and DDAB molecules at room temperature and the particles were dispersed in toluene. PbS and Au-PbS nanocrystals were synthesized according to hot-injection method.⁴⁶ Figure 4.1.1 shows TEM images of as-synthesized nanocrystals. The transmission electron microscopy image of (a) in figure 4.1.1 shows that gold nanocrystals with thiol ligands are monodispersed⁴⁵ and the average size of gold nanocrystals is approximately 4.5nm by metallic reduction reaction at

room temperature. In figure 4.1.1 (b), it shows PbS QDs capped with oleic-acid have nearly round shape with 3.0nm size. In figure 4.1.1 (c), as-synthesized Au/PbS core-shell nanostructures have square and thick PbS shells surrounding Au nanocrystals, but they have spherical shape structures with lower temperature.⁴⁶ The high crystallinity of core-shell nanostructures is shown in the high-resolution transmission electron microscopy (HRTEM) image in figure 4.1.1 (d).

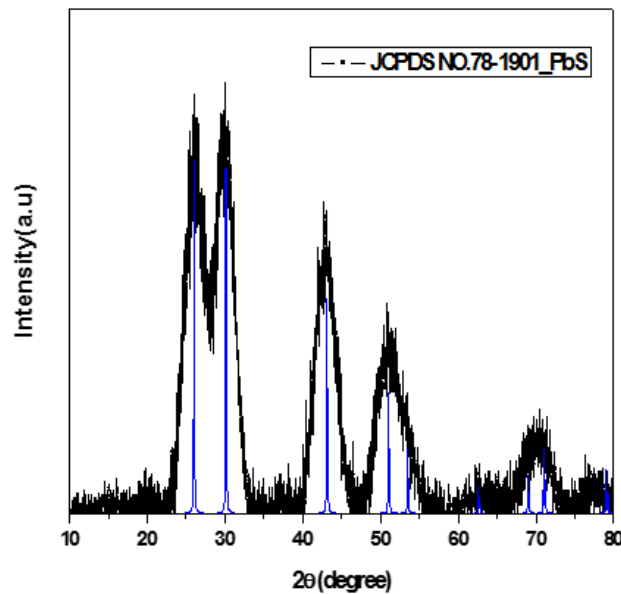


Figure 4.1.2. XRD patterns of PbS QDs coated on the glass substrates.

X-ray diffraction patterns of as-synthesized PbS QDs were identified with a standard JCPDS card no. 78-1901. The diffraction patterns from PbS QDs were broadend due to nano-sized particles. Several peaks are matched to (111), (200), (220), (311), (222), (400), (331), (420) and (422) crystal planes of cubic phase PbS at 2 theta values, approximately 26, 30, 43, 53 and others.

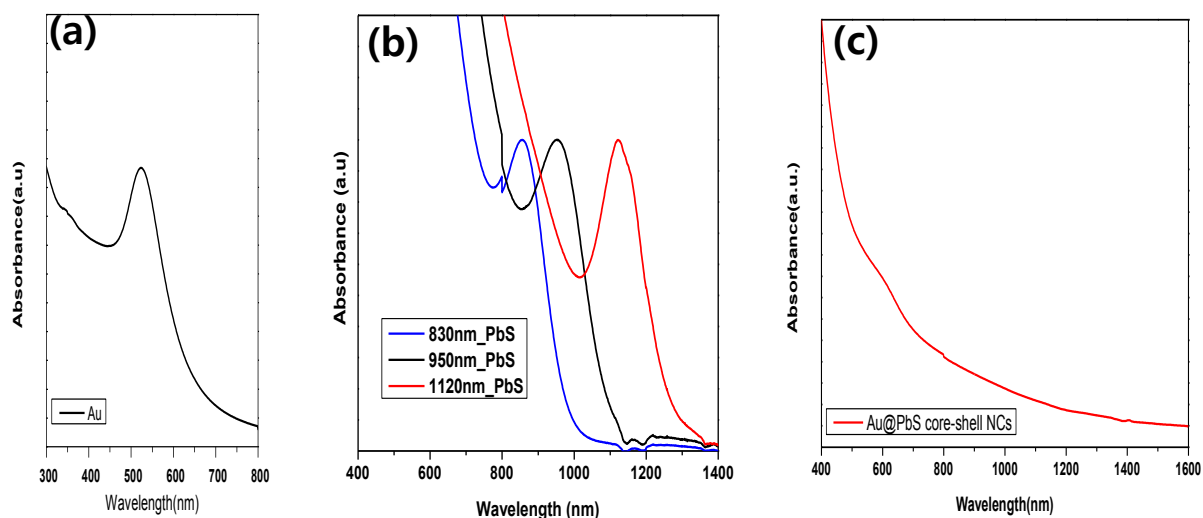


Figure 4.1.3. UV-vis-NIR spectra of (a) Au NCs, (b) PbS QDs with different absorption peaks and (c) Au-PbS core-shell NCs.

Figure 4.1.3 shows the absorption spectra of the Au nanocrystals, PbS QDs and Au-PbS core-shell nanostructures, respectively. In comparison with the previous reported nanostructures⁴⁶, PbS and Au-PbS nanostructures were not significantly monodispersed samples. The absorption peak of Gold nanoparticles appeared at around 530nm in the visible region due to surface plasmon resonance band related to electron-surface collisions in noble metals.⁴⁷ The first exciton absorption peaks of PbS QDs were shown at 830, 950 and 1120nm wavelengths, respectively. Those wavelengths approximately corresponded to optical band gaps of PbS QDs, 1.5eV, 1.3eV, 1.1eV, respectively. In figure 4.1.3 (c), as-synthesized Au-PbS core-shell nanostructures had broaden absorption wavelengths up to low-energy range and a strong p-doping effect due to the coupling between surface plasmons in the metal cores and generated excitons in the semiconducting shells, reported previously.⁴⁶ PbS and Au-PbS nanostructures would be expected to extract generated holes from perovskite layer.

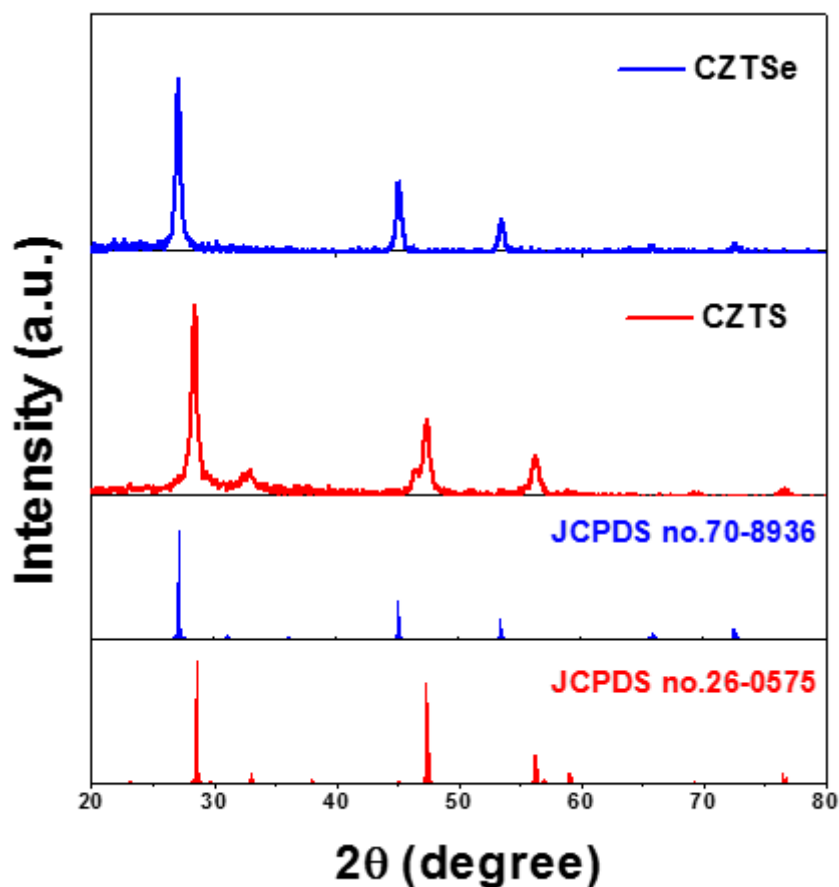


Figure 4.1.4. XRD patterns for as-synthesized $\text{Cu}_2\text{ZnSnSe}_4$ and $\text{Cu}_2\text{ZnSnS}_4$ nanocrystals on the glass substrates.

To find out structural characteristic, figure 4.1.4 indicates X-ray diffractions (XRD) patterns of the $\text{Cu}_2\text{ZnSnSe}_4$ (CZTSe) and $\text{Cu}_2\text{ZnSnS}_4$ (CZTS) quantum dots coated on the glass substrates. CZTSe quantum dots have shifted patterns compared to CZTS QDs, indicating that larger Se atoms changing lattice constants (a, c), Prieto et al.²⁴ The diffraction peak positions of CZTS are matched to (112), (200), (220), (312), (224), (008), (332) planes of the kesterite crystal. CZTS QDs are identified as kesterite crystal structures, JCPDS no.26-0575. The diffraction peak positions of $\text{Cu}_2\text{ZnSnSe}_4$, JCPDS no.70-8936, corresponds approximately to (112) at $2\Theta = 27.5^\circ$, (204) at $2\Theta = 45^\circ$, (312) at $2\Theta = 54^\circ$, (400) at $2\Theta = 66^\circ$, (316) planes at $2\Theta = 72.5^\circ$ of

kesterite crystal structure.

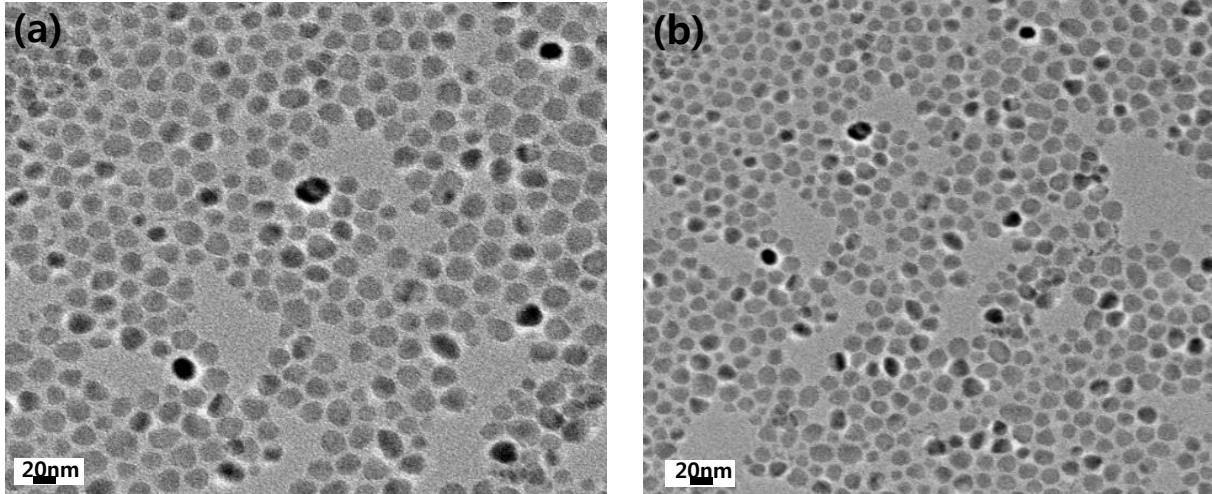


Figure 4.1.5. TEM images of (a) Cu₂ZnSnS₄ and (b) Cu₂ZnSnSe₄ quantum dots.

Transmission electron microscopy images in figure 4.1.5 shows the morphologies of as-synthesized CZTS and CZTSe QDs capped with Trioctylphosphine oxide (TOPO) and oleylamine (OLA) ligands and dispersed in toluene. Those QDs had almost circle shape and average diameter in the range of 10-20nm. As previously reported by Amy L. Prieto et al,²⁴ the portion of selenium element affected particle diameter.

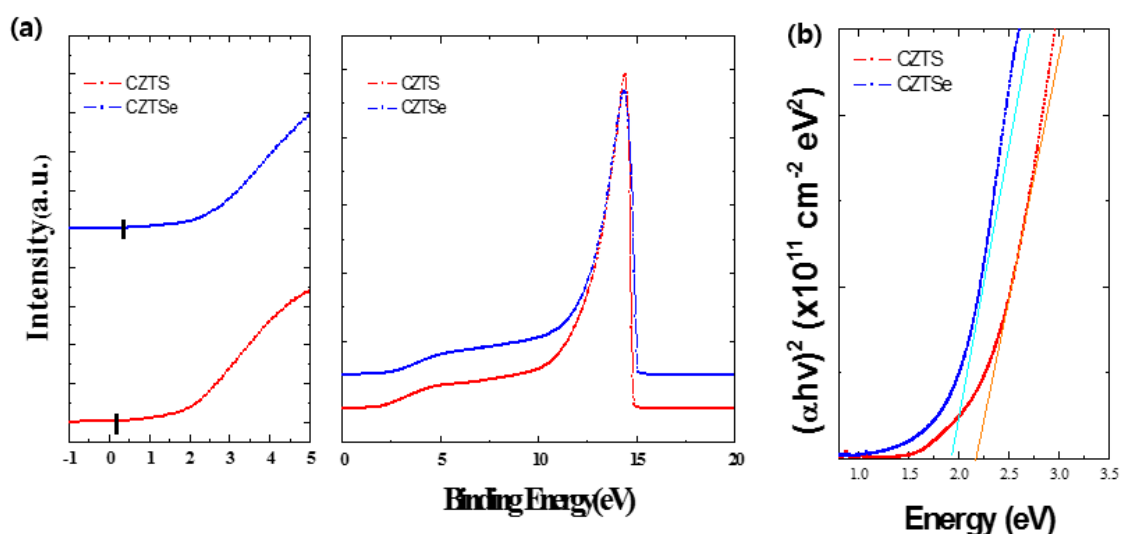


Figure 4.1.6. (a) UPS spectrum of as-deposited CZTS and CZTSe nanocrystal films on the glass substrate, (left) the valence band edge in the short-range binding energy, (right) general UPS spectrum. (b) $(\alpha h\nu)^2$ vs energy plots where CZTS and CZTSe nanocrystal films are determined to be 2.2eV and 1.92eV respectively.

We carried out using UPS and UV-vis-NIR spectroscopy to determine electronic structure of CZTS and CZTSe QDs. As consulting some references,^{15,48} the workfunction of each quantum dot was determined based on high binding energy onset and low binding energy onset respectively. We could calculate optical band gap of CZTS and CZTSe QDs from UV-vis-NIR measurement. CZTS QDs have the workfunction of 5.23 eV and band gap of 2.2 eV yielding the conduction band edge of 3.03 eV. CZTSe QDs have also the workfunction of 5.11 eV and band gap of 1.9 eV, yielding the conduction band edge of 3.21 eV.

Table 4.1. valence and conduction band edge of CZTS and CZTSe QDs

Sample	E_{valence}	$E_{\text{conduction}}$	E_g
CZTS QDs	5.23 eV	3.03 eV	2.2 eV
CZTSe QDs	5.11 eV	3.21 eV	1.9 eV

4.2 Characterization of perovskite films

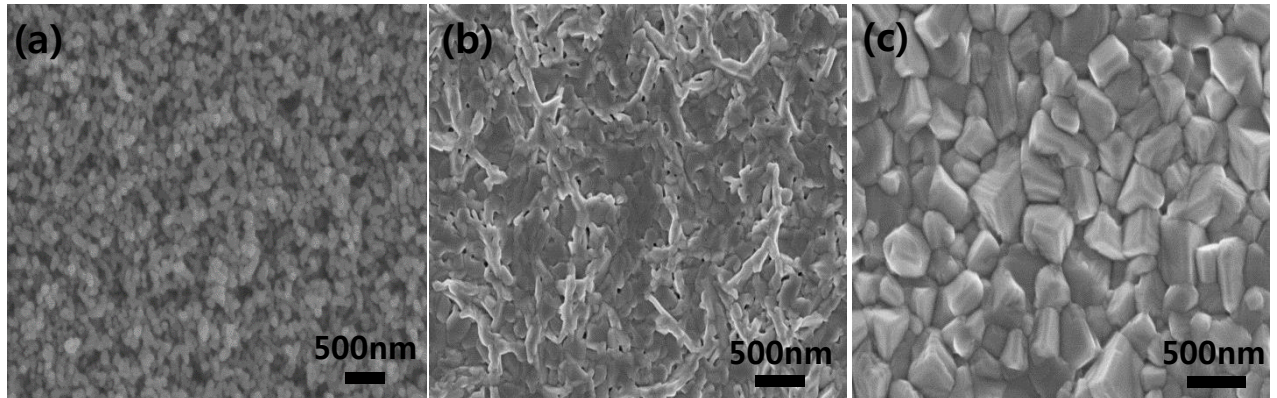


Figure 4.2.1. Top view SEM images of (a) mesoporous TiO₂ (30nm) films, (b) PbI₂ films on mesoporous TiO₂ layer and (c) CH₃NH₃PbI₃ perovskite films with 10mg/ml MAI solution.

We fabricated perovskite solar cells using modified two-step deposition⁴⁰ by spin-coating. As shown in figure 4.2.1, scanning electron microscopy images showed the formation of perovskite films and the morphology of perovskite films. When the PbI₂ crystals were converted to the perovskite crystals, the morphology and crystal size of the perovskite film was controlled by the concentration of methylammonium iodide (MAI) precursors dissolved in 2-propanol.^{44,49} Our deposition process was optimized on 30nm TiO₂ mesoporous layer (about 400nm thickness) shown at figure 4.2.1 (a). The cuboid shapes of the perovskite crystal film were fabricated densely using 1M PbI₂ and MAI-IPA solution (10mg/ml) and led to the rough surface of the perovskite layer on the mesoporous TiO₂ layer. The crystal dimension for CH₃NH₃PbI₃ domains was in the range of more than 100nm.

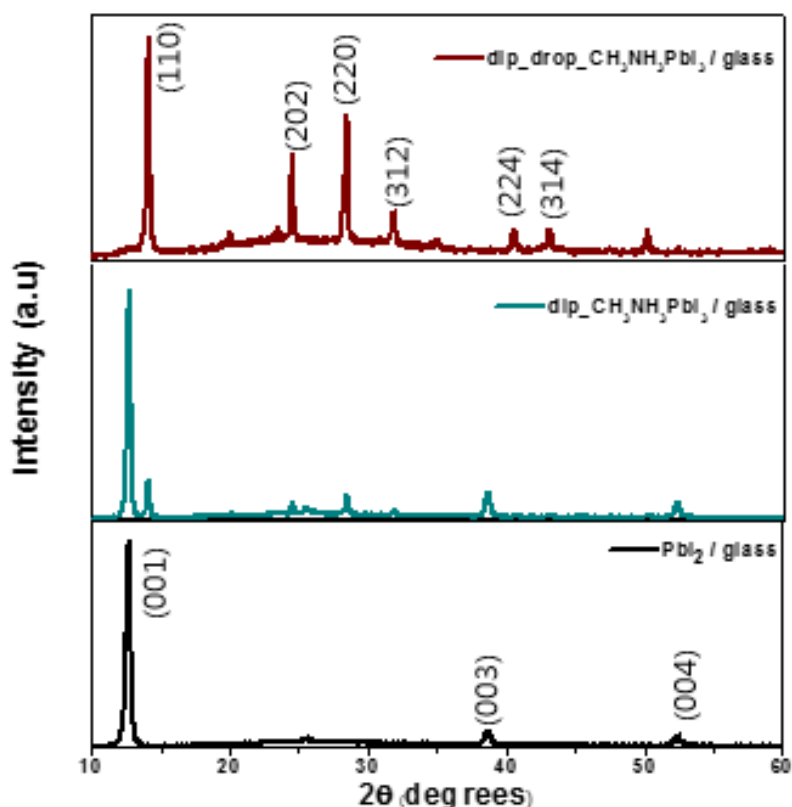


Figure 4.2.2. XRD patterns of PbI₂ and CH₃NH₃PbI₃ films on the glass substrates.

Figure 4.2.2 shows XRD patterns of PbI₂ and CH₃NH₃PbI₃ films corresponding to the reference.⁵⁰ The peaks of PbI₂ film correlated with hexagonal 2H polytype crystal structure indexes.³⁶ A main peak of PbI₂ corresponds to (001) crystal plane. After dipping process to form MAPbI₃ crystal films, the conversion of PbI₂ into MAPbI₃ perovskite crystals was not complete. Additional dropping MAI-IPA solution during fabrication contributed to form more MAPbI₃ crystal structures of which the peaks correspond to (110), (220) crystal planes in the tetragonal structure. Three films were not composed of mesoporous TiO₂ layer, which causes different XRD patterns due to infiltrated crystalline PbI₂.

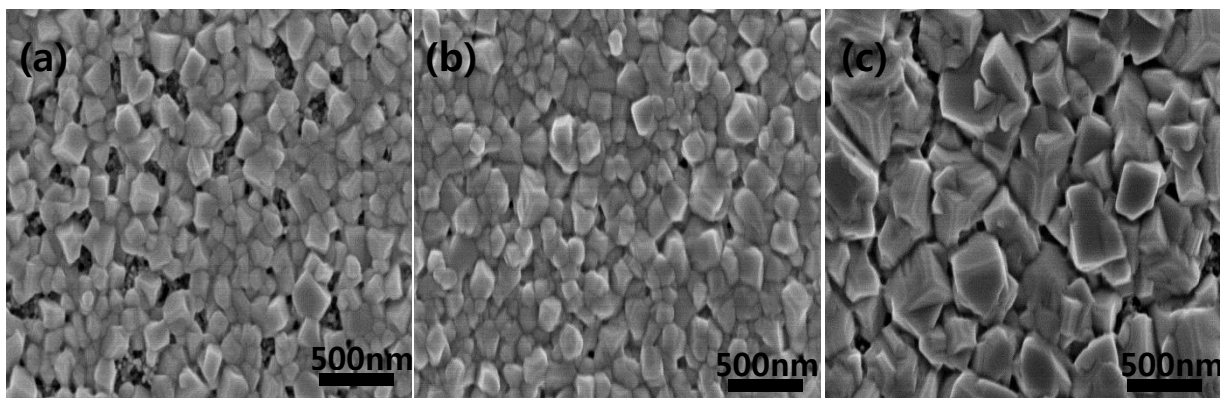


Figure 4.2.3. Top-view SEM images of the perovskite film with different heat treatments on the pre-heated mesoscopic layer. (a) room temperature (b) 50 °C and (c) 70 °C glass coated on TiO₂

Pre or post-heating treatment influenced the formation of organometal halide perovskite thin films. Before depositing the perovskite layer, pre-heating treatment in two-step deposition was important to make dense perovskite film and affected the growth of perovskite domains. Figure 4.2.3 shows that PbI₂ substrates coated on the TiO₂ layer depending on different pre-annealing treatment changed crystallinity of CH₃PbI₃ thin films. As increasing pre-annealing temperature, the bigger CH₃NH₃PbI₃ crystals appeared and close-packed films formed. It was reported that pre-annealing treatment helped to increase perovskite size and enhance crystallinity of CH₃NH₃PbI₃ crystals.⁵¹ The pin-hole free devices were fabricated at 50 °C pre-heated glasses.

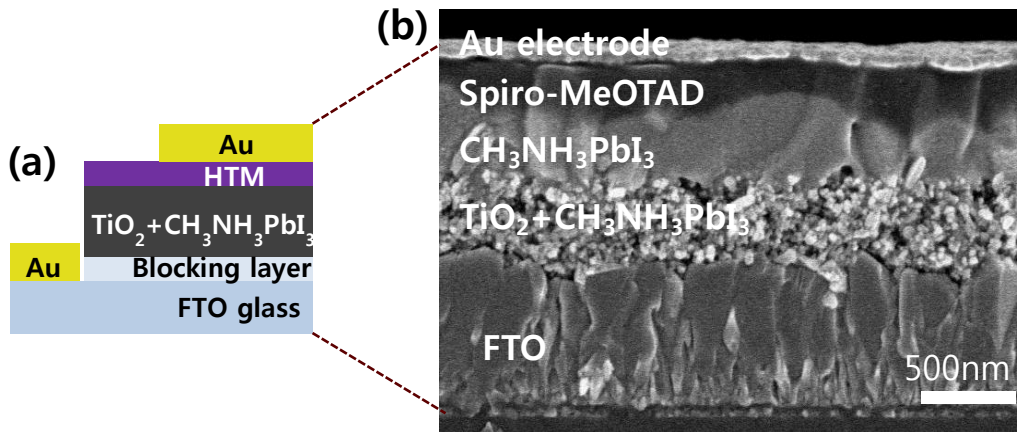


Figure 4.2.4. (a) Schematic structure of the device. (b) Cross-sectional SEM image of TiO₂ / CH₃NH₃PbI₃ / Spiro-MeOTAD / Au.

Figure 4.2.4 (a) shows a schematic structure of the device consisting mesoscopic perovskite layer, spiro-MeOTAD and gold electrodes. The blocking layer (TiO₂), which indicates 30nm thickness, was spray-coated at 500°C to prevent holes formed in perovskite layer from reaching the fluorine doped tin oxide (FTO) electrode and. The thickness of the mesoscopic perovskite layer as an absorption layer was about 400nm thickness and upper perovskite layer on the TiO₂ layer was 200nm thickness. Spiro-MeOTAD as hole-conducting materials, which has -5.22 eV HOMO level suitable for transporting holes, was average 150nm thickness and gold electrode was thermally evaporated with back contacts as shown in figure 4.2.2 (b).

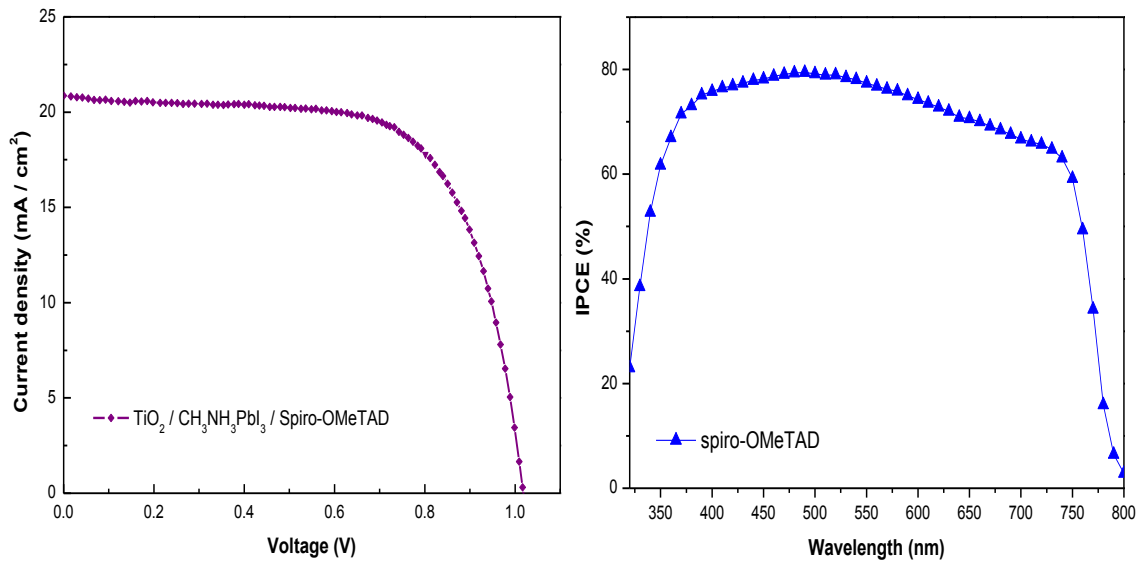


Figure 4.2.5. (a) Current density-Voltage curve of $\text{CH}_3\text{NH}_3\text{PbI}_3$ device with spiro-MeOTAD under AM 1.5G spectrum (100mW cm^{-2}) in the air (b) IPCE spectrum of the device with spiro-MeOTAD in the air.

Table 4.2. Photovoltaic parameters for the perovskite solar cell with Spiro-MeOTAD

Cell type	V_{oc} (V)	J_{sc} (mA / cm^2)	FF	PCE(%)
$\text{TiO}_2 / \text{CH}_3\text{NH}_3\text{PbI}_3 /$ Spiro-MeOTAD / Au	1.01	20.86	67.0	14.2

Figure 4.2.5 shows how efficient perovskite solar cells employing Spiro-MeOTAD were fabricated under 100mW/cm^2 irradiation and how efficiently incident photons were converted into charge carriers or photocurrent in accordance with generated wavelengths, respectively. Photovoltaic parameters for the perovskite solar cell with Spiro-MeOTAD were gathered in table 1. The solar cell based on $\text{TiO}_2 / \text{CH}_3\text{NH}_3\text{PbI}_3 / \text{Spiro-MeOTAD} / \text{Au}$ exhibited the highest open circuit voltage (V_{oc}) of 1.01 V at a forward bias, photocurrent density (J_{sc}) of 20.86 mA/cm^2 , fill factor (FF) of 67% and the maximum power conversion efficiency (PCE) of 14.2%. The IPCE spectrum of the device reached over 70% in the range of 400 to 800nm.

These values are not slightly different from the reference⁴⁰ due to different TiO₂ nanoparticle size and the thickness of TiO₂ layer.

4.3 Characterization of perovskite solar cells with nanocrystals

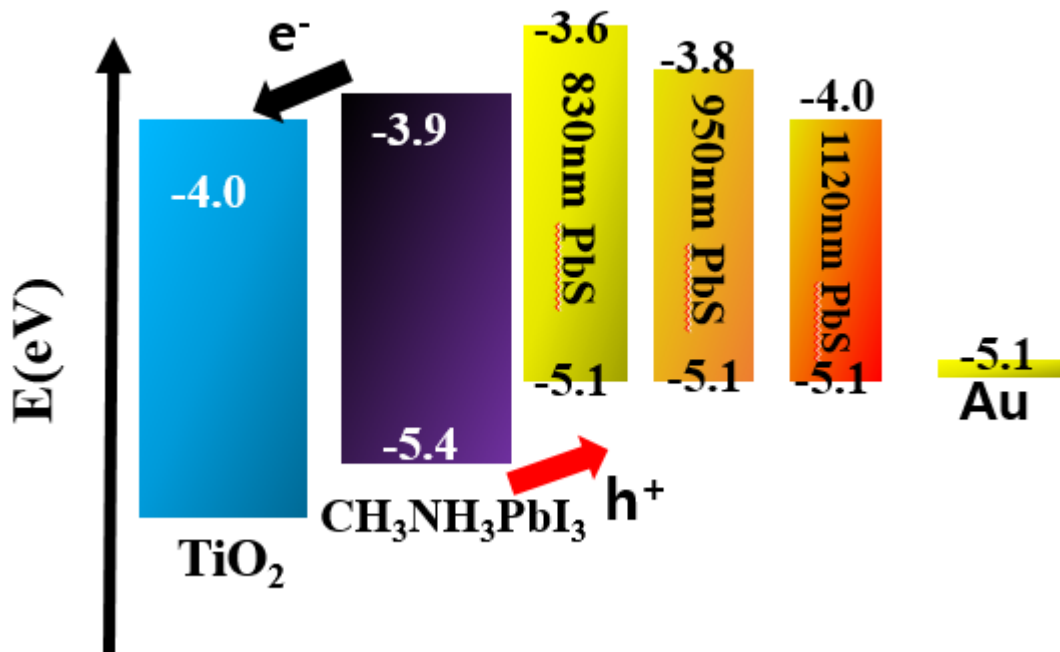


Figure 4.3.1. Energy level diagram of TiO₂ / CH₃NH₃PbI₃ / PbS QDs / Au

The energy band diagram demonstrates band levels of each layer based on work function illustrated in the reference. The electronic structures of CH₃NH₃PbI₃ were generally known as band gap was 1.5 eV, valence band edge was -5.43 eV and conduction band edge was -3.93 eV.³ TiO₂ as n-type semiconductor was generally known as -4.0 eV and PbS QDs⁵² could be easily tuned to be suitable for perovskite band levels. As shown figure 4.3.1, generated electron-hole pairs in the perovskite layer transfer from CH₃NH₃PbI₃ to TiO₂ or PbS QDs with different band alignments. It is expected that generated electron-hole pairs in the PbS QDs

could transfer from PbS QDs to lower band positions²⁰ and PbS QDs layer block the electron injection from perovskite layer into PbS QDs.

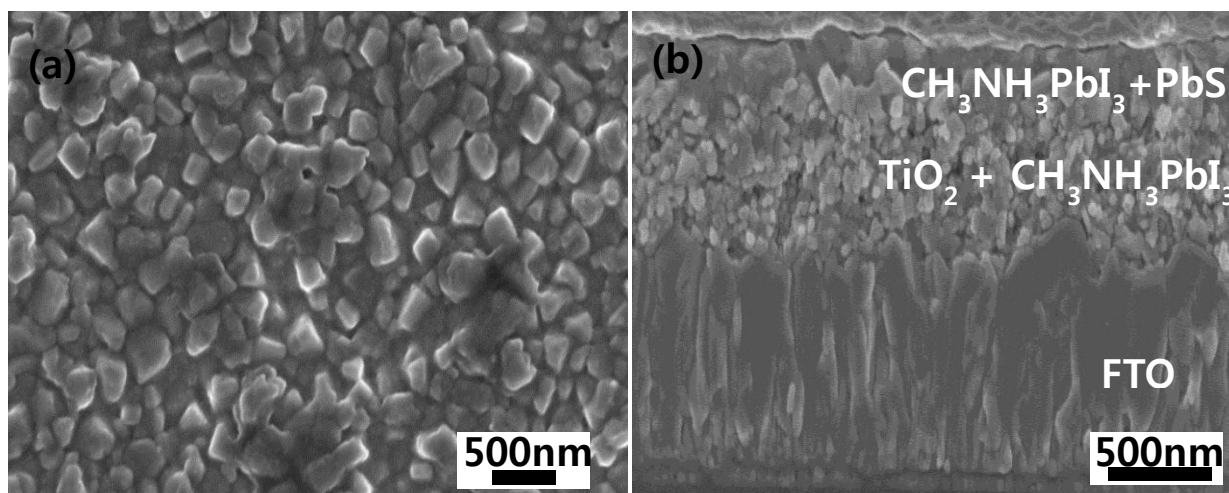


Figure 4.3.2. Top view SEM image of (a) PbS-coated perovskite films. Cross-sectional SEM image of $\text{TiO}_2 / \text{CH}_3\text{NH}_3\text{PbI}_3 / \text{PbS QDs} / \text{Au}$

After depositing mesoscopic perovskite layer on the substrates, we spin-coated PbS QDs dispersed in the non-polar solvent like octane. Figure 4.3.2 shows top view SEM image of PbS-coated perovskite film and cross-sectional image of the device. Cuboid-shaped perovskite crystals are partially covered with PbS QDs which filled pores between perovskite crystals corresponding to smooth gold electrodes. The QD layer thickness is around 10 to 15nm

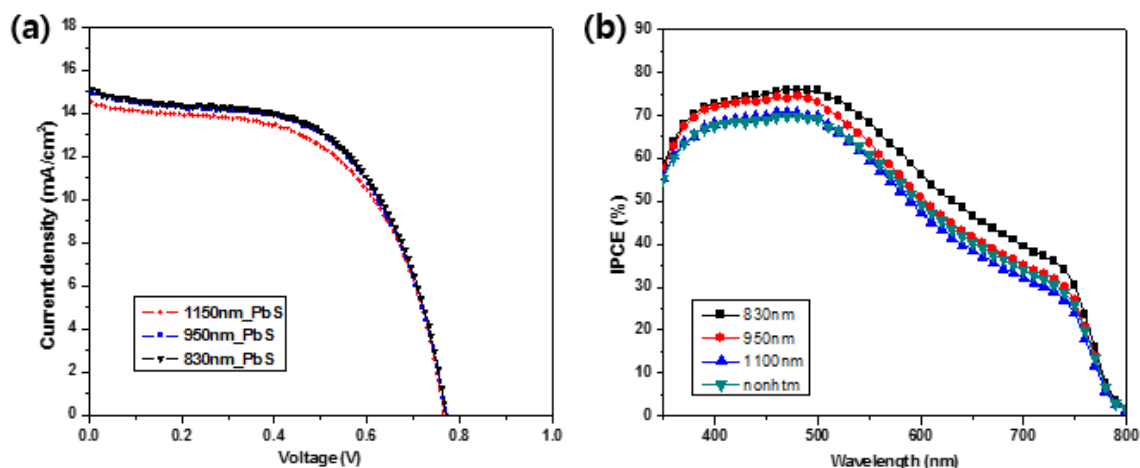


Figure 4.3.3. Current density-Voltage curve of $\text{CH}_3\text{NH}_3\text{PbI}_3$ device with different sizes of PbS QDs under AM 1.5G spectrum (100mW cm^{-2}) in the air (b) IPCE spectrum of the device with different sized PbS QDs.

To demonstrate different sized PbS QDs for the hole-transporting material in perovskite solar cells we characterized them using J-V curve measurement and incident photon to conversion efficiency or EQE measurement. Based on the hole-free device, different sized quantum dot based perovskite solar cells has enhanced current density but reduced open-circuit voltage. V_{oc} and fill factor are related to charge carrier recombination and interface between layers. Long chain organic molecules capping quantum dots and incomplete interface between perovskite and QD layers may lead to reduce V_{oc} . Enhanced current density implies PbS QDs could help to extract or collect holes generated from perovskite layer through IPCE spectra. We also characterized Au-PbS based perovskite solar cells. But the performances of the devices were not lower than PbS based perovskite solar cells due to unexpected reasons.

Table 4.3. Photovoltaic parameters for perovskite solar cell with different sized PbS QDs

Cell type	V_{oc} (V)	J_{sc} (mA / cm^2)	FF	PCE(%)
830nm	0.77	15.00	58.1	6.7
950nm	0.77	15.15	58.0	6.7
1120nm	0.76	14.57	57.4	6.4

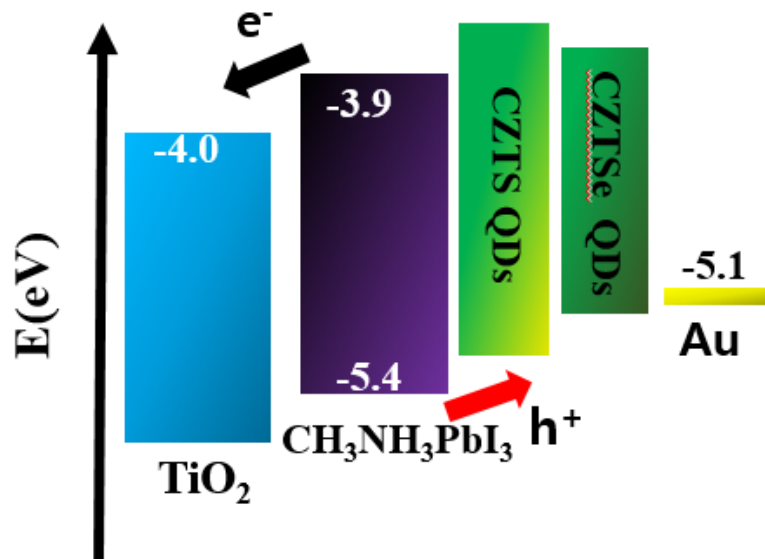


Figure 4.3.4. Energy level alignment for CZTS and CZTSe QDs based perovskite solar cell

We could illustrate energy level alignment for CZTS and CZTSe QDs employed in the mesoscopic perovskite solar cell through previous UPS and UV-vis-NIR measurements. The valence band edge of CZTS (-5.23 eV) and CZTSe (-5.11 eV) QDs is located at a higher position based on the valence band edge of -5.4 eV MAPbI₃, leading to collect holes generated from the perovskite layer easily. The conduction band edge of CZTS (-3.03 eV) and CZTSe (-3.11 eV) QDs lies at a higher position based on CH₃NH₃PbI₃, which indicates that it blocks the electron injection from the CH₃NH₃PbI₃ layer into the QDs layer related to charge recombination.

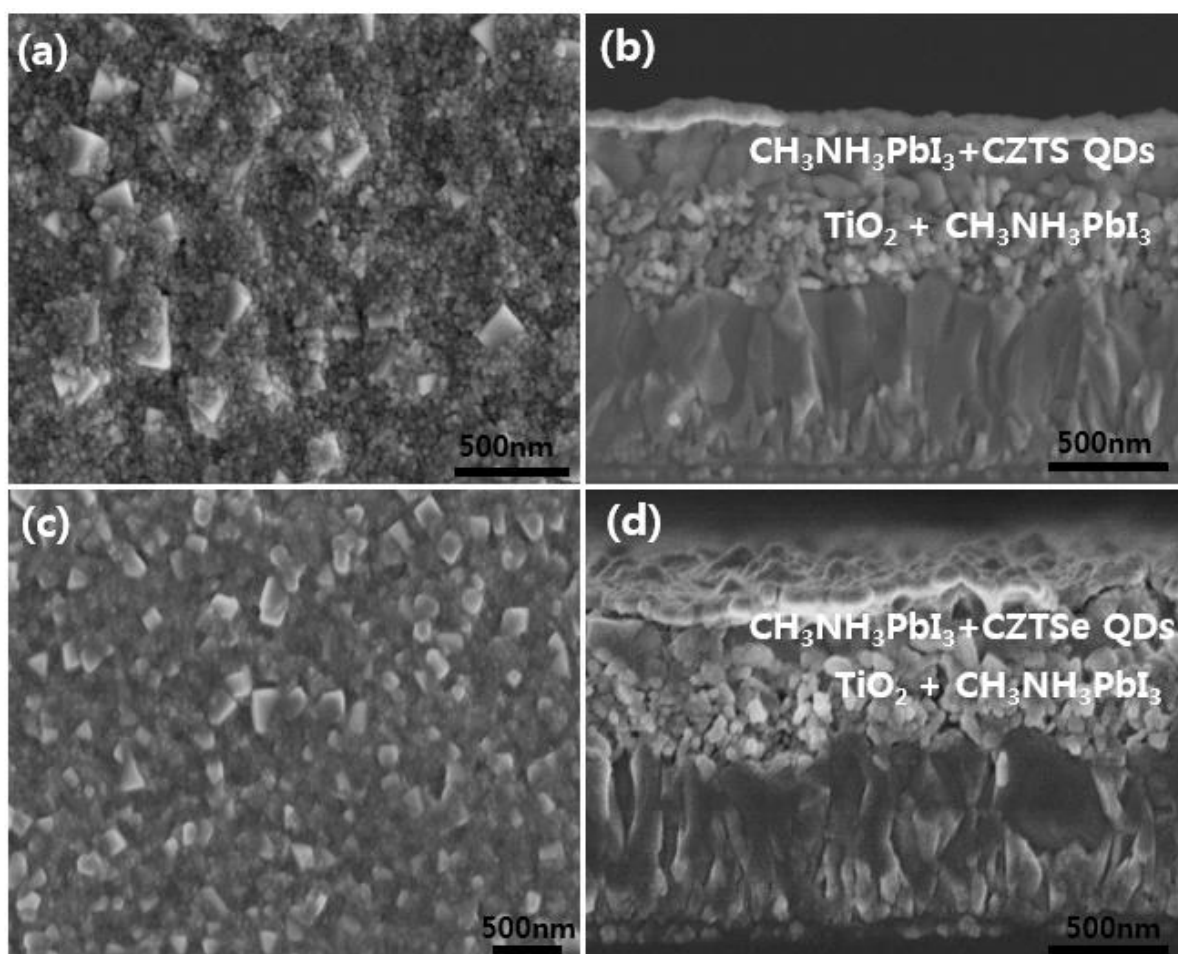


Figure 4.3.5. Top-view (a, c) and cross-sectional (b, d) scanning electron microscopy (SEM) images of the devices based on MAPbI₃ perovskite layers by two-step deposition method. CZTS quantum dots coated on the perovskite layer (a, b) and CZTSe quantum dots coated on the perovskite layer (b, d).

After depositing mesoscopic perovskite layer through dipping and dropping process, we spin-coated CZTS and CZTSe QDs on the film. Those QDs filled vacancies between cuboid-shaped perovskite crystals leading to smooth the surface of gold electrode. The perovskite crystals were partially covered with CZTS and CZTSe quantum dots as shown figure 10a and c. cross-sectional images of the devices as shown (b) and (c) shows each layer thickness. Among there layers, the layer of CZTS and CZTSe QDs coated on the perovskite layer is in the range of 20 to 30nm thickness.

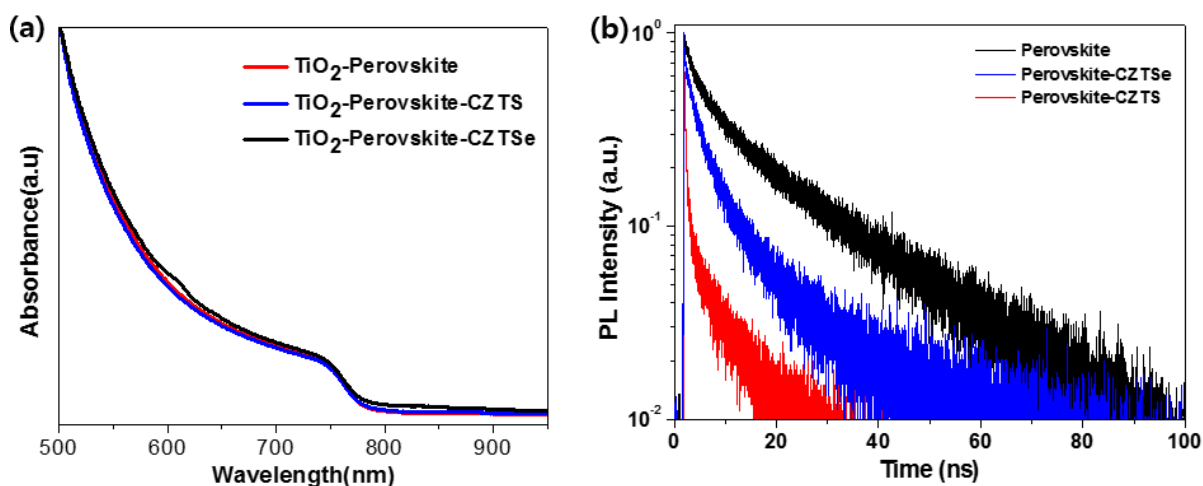


Figure 4.3.6. UV-Vis-NIR absorption spectra for different types of films. TiO_2 / $\text{CH}_3\text{NH}_3\text{PbI}_3$, TiO_2 / $\text{CH}_3\text{NH}_3\text{PbI}_3$ / CZTS QDs and TiO_2 / $\text{CH}_3\text{NH}_3\text{PbI}_3$ / CZTSe QDs. (b) Normalized time-resolved photoluminescence decay aspects of perovskite films with different hole-conducting materials.

UV-vis-NIR absorption spectra and time-resolved photoluminescence (TRPL) decay were performed to understand the role of CZTS and CZTSe QDs in the perovskite solar cell. Figure 10a shows the absorption spectra of three types of films on the mesoporous TiO_2 layer. We expected that those quantum dots could enhance the absorption of the perovskite film or extend absorption range of the perovskite material. However, it might be too thin thickness of QDs layer to enhance absorption of the films for broad wavelengths. Time-resolved photoluminescence decay spectra were performed to investigate hole-extraction dynamics. CZTS and CZTSe coated on $\text{CH}_3\text{NH}_3\text{PbI}_3$ film could be more effective PL quenched compared to only perovskite film and CZTS QDs would be efficient hole-extracting materials in comparison with CZTSe QDs based perovskite film.

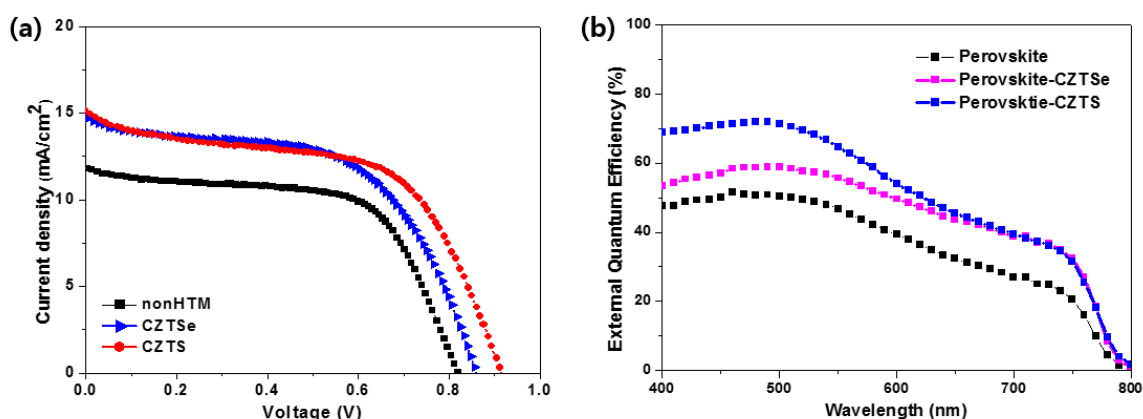


Figure 4.3.7. (a) Current-Voltage curves of CH₃NH₃PbI₃ devices with different hole-conducting layers measured under AM 1.5G illumination(100mW cm⁻²) in the air. (b) External quantum efficiency spectra of solar cells measured in the air.

To demonstrate CZTS and CZTSe QDs for the hole-transporting material in the perovskite solar cell, we measured current density-voltage (J-V) curves under AM 1.5G illumination in the air and incident-photon-to-conversion efficiency (IPCE) spectrum and summarized photovoltaic parameters in table 3. With hole-free device, the PCE of 5.9% with a V_{oc} of 0.81 V, a J_{sc} of 12.7 mA / cm², a FF of 56.7% was obtained. With CZTS QDs based perovskite solar cell, the highest PCE of 7.6% with a V_{oc} of 0.88 V, a J_{sc} of 15.56 mA / cm², a FF of 55.4% was achieved. With CZTSe QDs based perovskite solar cell, the highest PCE of 7.6% with a V_{oc} of 0.88 V, a J_{sc} of 15.56 mA / cm², a FF of 55.4% was achieved. It was reported that lower HOMO level of hole-transporting materials became higher V_{oc} of mesoscopic perovskite solar cells. CZTS QDs based perovskite solar cell has higher V_{oc} because of lower valence band edge than CZTSe QDs as measured UPS data. These QDs based perovskite solar cells exhibit enhanced current density compared with the hole-free device due to contribution to hole extraction generated from perovskite layer as shown IPCE spectra

Table 4.4. Photovoltaic parameters for different HTMs of perovskite solar cells

Cell type	V _{oc} (V)	J _{sc} (mA / cm ²)	FF	PCE(%)
TiO ₂ / CH ₃ NH ₃ PbI ₃ / CZTS QDs / Au	0.88	15.56	55.4	7.6
TiO ₂ / CH ₃ NH ₃ PbI ₃ / CZTSe QDs/ Au	0.85	15.13	55.1	7.1
TiO ₂ / CH ₃ NH ₃ PbI ₃ / Au	0.81	12.7	56.7	5.9

5. Summary & Conclusion

In summary, we have synthesized PbS, Au-PbS, CZTS, CZTSe QDs by hot-injection method and fabricated perovskite solar cells with colloidal quantum dot nanocrystals for hole-transporting materials. PbS QDs, which have different optical band gap according to size and high absorption coefficient and low cost compared to organic conducting polymers, were spin-coated on n-i-p mesoscopic perovskite layer by solution-processed method. The devices with different sized PbS QDs exhibit enhanced current density and reduced open-circuit voltage and the maximum power conversion efficiency reaches 6.7%. we also applied Au-PbS core-shell nanocrystals to the hole-transporting layer in the perovskite solar cell due to the relation between plasmon and exciton resulting in strong p-type doping effect but the performances of the devices were not generally reduced compared with PbS based perovskite solar cells due to incomplete process.

Cu-based CZTS and CZTSe QDs as synthesized by hot-injection method exhibit different electronic structures according to S or Se element and enhanced photovoltaic parameters in comparison with hole-free devices. It shows that CZTS (or Se) QDs can assist extraction or collection of holes generated from perovskite layer and CZTS QDs are more efficient hole extractor compared to CZTSe QDs through IPCE measurement and lower valence band edge of CZTS QDs leads to higher open-circuit voltage of mesoscopic perovskite solar cells. Colloidal quantum dots can be potential to enhance photovoltaic performance in mesoscopic perovskite solar cells as hole-transporting materials through optimizing thickness and modifying ligands.

6. Reference

1. Kojima, A.; Teshima, K.; Shirai, Y.; Miyasaka, T., Organometal Halide Perovskites as Visible-Light Sensitizers for Photovoltaic Cells. *Journal of the American Chemical Society* **2009**, *131* (17), 6050-6051.
2. Im, J.-H.; Lee, C.-R.; Lee, J.-W.; Park, S.-W.; Park, N.-G., 6.5% efficient perovskite quantum-dot-sensitized solar cell. *Nanoscale* **2011**, *3* (10), 4088-4093.
3. Kim, H.-S.; Lee, C.-R.; Im, J.-H.; Lee, K.-B.; Moehl, T.; Marchioro, A.; Moon, S.-J.; Humphry-Baker, R.; Yum, J.-H.; Moser, J. E.; Gratzel, M.; Park, N.-G., Lead Iodide Perovskite Sensitized All-Solid-State Submicron Thin Film Mesoscopic Solar Cell with Efficiency Exceeding 9%. *Sci. Rep.* **2012**, *2*.
4. Hao, F.; Stoumpos, C. C.; Cao, D. H.; Chang, R. P. H.; Kanatzidis, M. G., Lead-free solid-state organic-inorganic halide perovskite solar cells. *Nat Photon* **2014**, *8* (6), 489-494;
5. Heo, J. H.; Im, S. H.; Noh, J. H.; Mandal, T. N.; Lim, C.-S.; Chang, J. A.; Lee, Y. H.; Kim, H.-j.; Sarkar, A.; Nazeeruddin, M. K.; Gratzel, M.; Seok, S. I., Efficient inorganic-organic hybrid heterojunction solar cells containing perovskite compound and polymeric hole conductors. *Nat Photon* **2013**, *7* (6), 486-491.
6. Saliba, M.; Matsui, T.; Seo, J.-Y.; Domanski, K.; Correa-Baena, J.-P.; Nazeeruddin, M. K.; Zakeeruddin, S. M.; Tress, W.; Abate, A.; Hagfeldt, A.; Gratzel, M., Cesium-containing triple cation perovskite solar cells: improved stability, reproducibility and high efficiency. *Energy & Environmental Science* **2016**.
7. Seo, J.; Noh, J. H.; Seok, S. I., Rational Strategies for Efficient Perovskite Solar Cells. *Accounts of Chemical Research* **2016**, *49* (3), 562-572.
8. Noh, J. H.; Jeon, N. J.; Choi, Y. C.; Nazeeruddin, M. K.; Gratzel, M.; Seok, S. I., Nanostructured TiO₂/CH₃NH₃PbI₃ heterojunction solar cells employing spiro-OMeTAD/Co-complex as hole-transporting material. *Journal of Materials Chemistry A* **2013**, *1* (38), 11842-11847.
9. Li, M.-H.; Shen, P.-S.; Wang, K.-C.; Guo, T.-F.; Chen, P., Inorganic p-type contact materials for perovskite-based solar cells. *Journal of Materials Chemistry A* **2015**, *3* (17), 9011-9019.
10. Qin, P.; Tanaka, S.; Ito, S.; Tetreault, N.; Manabe, K.; Nishino, H.; Nazeeruddin, M. K.; Grätzel, M., Inorganic hole conductor-based lead halide perovskite solar cells with 12.4% conversion efficiency. *Nat Commun* **2014**, *5*.
11. Christians, J. A.; Fung, R. C. M.; Kamat, P. V., An Inorganic Hole Conductor for Organo-Lead Halide Perovskite Solar Cells. Improved Hole Conductivity with Copper Iodide. *Journal of the American Chemical Society* **2014**, *136* (2), 758-764.
12. Zhang, Y.; Liu, M.; Eperon, G. E.; Leijtens, T. C.; McMeekin, D.; Saliba, M.; Zhang, W.; de Bastiani, M.; Petrozza, A.; Herz, L. M.; Johnston, M. B.; Lin, H.; Snaith, H. J., Charge selective contacts, mobile ions and anomalous hysteresis in organic-inorganic perovskite solar cells. *Materials Horizons* **2015**, *2* (3), 315-322.
13. Etgar, L.; Gao, P.; Qin, P.; Gratzel, M.; Nazeeruddin, M. K., A hybrid lead iodide perovskite and

- lead sulfide QD heterojunction solar cell to obtain a panchromatic response. *Journal of Materials Chemistry A* **2014**, *2* (30), 11586-11590.
14. Hu, L.; Wang, W.; Liu, H.; Peng, J.; Cao, H.; Shao, G.; Xia, Z.; Ma, W.; Tang, J., PbS colloidal quantum dots as an effective hole transporter for planar heterojunction perovskite solar cells. *Journal of Materials Chemistry A* **2015**, *3* (2), 515-518.
15. Wang, L.; Fu, W.; Gu, Z.; Fan, C.; Yang, X.; Li, H.; Chen, H., Low temperature solution processed planar heterojunction perovskite solar cells with a CdSe nanocrystal as an electron transport/extraction layer. *Journal of Materials Chemistry C* **2014**, *2* (43), 9087-9090.
16. Yu, W.; Li, F.; Wang, H.; Alarousu, E.; Chen, Y.; Lin, B.; Wang, L.; Hedhili, M. N.; Li, Y.; Wu, K.; Wang, X.; Mohammed, O. F.; Wu, T., Ultrathin Cu₂O as an efficient inorganic hole transporting material for perovskite solar cells. *Nanoscale* **2016**, *8* (11), 6173-6179.
17. Rao, H.; Sun, W.; Ye, S.; Yan, W.; Li, Y.; Peng, H.; Liu, Z.; Bian, Z.; Huang, C., Solution-Processed CuS NPs as an Inorganic Hole-Selective Contact Material for Inverted Planar Perovskite Solar Cells. *ACS Applied Materials & Interfaces* **2016**.
18. Wu, Q.; Xue, C.; Li, Y.; Zhou, P.; Liu, W.; Zhu, J.; Dai, S.; Zhu, C.; Yang, S., Kesterite Cu₂ZnSnS₄ as a Low-Cost Inorganic Hole-Transporting Material for High-Efficiency Perovskite Solar Cells. *ACS Applied Materials & Interfaces* **2015**, *7* (51), 28466-28473;
19. Zhao, N.; Osedach, T. P.; Chang, L.-Y.; Geyer, S. M.; Wanger, D.; Binda, M. T.; Arango, A. C.; Bawendi, M. G.; Bulovic, V., Colloidal PbS Quantum Dot Solar Cells with High Fill Factor. *ACS Nano* **2010**, *4* (7), 3743-3752;
20. Chuang, C.-H. M.; Brown, P. R.; Bulović, V.; Bawendi, M. G., Improved performance and stability in quantum dot solar cells through band alignment engineering. *Nat Mater* **2014**, *13* (8), 796-801.
21. Yoon, W.; Boercker, J. E.; Lumb, M. P.; Placencia, D.; Foos, E. E.; Tischler, J. G., Enhanced Open-Circuit Voltage of PbS Nanocrystal Quantum Dot Solar Cells. *Sci. Rep.* **2013**, *3*.
22. Li, Y.; Zhu, J.; Huang, Y.; Wei, J.; Liu, F.; Shao, Z.; Hu, L.; Chen, S.; Yang, S.; Tang, J.; Yao, J.; Dai, S., Efficient inorganic solid solar cells composed of perovskite and PbS quantum dots. *Nanoscale* **2015**, *7* (21), 9902-9907.
23. Dai, P.; Shen, X.; Lin, Z.; Feng, Z.; Xu, H.; Zhan, J., Band-gap tunable (Cu₂Sn)_{x/3}Zn_{1-x}S nanoparticles for solar cells. *Chemical Communications* **2010**, *46* (31), 5749-5751.
24. Riha, S. C.; Parkinson, B. A.; Prieto, A. L., Compositionally Tunable Cu₂ZnSn(S_{1-x}Se_x)₄ Nanocrystals: Probing the Effect of Se-Inclusion in Mixed Chalcogenide Thin Films. *Journal of the American Chemical Society* **2011**, *133* (39), 15272-15275.
25. Murray, C. B.; Norris, D. J.; Bawendi, M. G., Synthesis and characterization of nearly monodisperse CdE (E = sulfur, selenium, tellurium) semiconductor nanocrystallites. *Journal of the American Chemical Society* **1993**, *115* (19), 8706-8715.
26. Rogach, A. L., *Semiconductor Nanocrystal Quantum Dots*. SpringerWienNewYork: 2008.
27. Park, J.; An, K.; Hwang, Y.; Park, J.-G.; Noh, H.-J.; Kim, J.-Y.; Park, J.-H.; Hwang, N.-M.; Hyeon, T., Ultra-large-scale syntheses of monodisperse nanocrystals. *Nat Mater* **2004**, *3* (12), 891-895.

28. Talapin, D. V.; Lee, J.-S.; Kovalenko, M. V.; Shevchenko, E. V., Prospects of Colloidal Nanocrystals for Electronic and Optoelectronic Applications. *Chemical Reviews* **2009**, *110* (1), 389-458.
29. Park, N.-G., Perovskite solar cells: an emerging photovoltaic technology. *Materials Today* **2015**, *18* (2), 65-72.
30. Green, M. A.; Ho-Baillie, A.; Snaith, H. J., The emergence of perovskite solar cells. *Nat Photon* **2014**, *8* (7), 506-514.
31. Snaith, H. J., Perovskites: The Emergence of a New Era for Low-Cost, High-Efficiency Solar Cells. *The Journal of Physical Chemistry Letters* **2013**, *4* (21), 3623-3630.
32. Liyan, Y.; Alexander, T. B.; David, G. L.; Tao, W., Recent progress and challenges of organometal halide perovskite solar cells. *Reports on Progress in Physics* **2016**, *79* (2), 026501.
33. Jeon, N. J.; Noh, J. H.; Yang, W. S.; Kim, Y. C.; Ryu, S.; Seo, J.; Seok, S. I., Compositional engineering of perovskite materials for high-performance solar cells. *Nature* **2015**, *517* (7535), 476-480.
34. Eperon, G. E.; Paterno, G. M.; Sutton, R. J.; Zampetti, A.; Haghighirad, A. A.; Cacialli, F.; Snaith, H. J., Inorganic caesium lead iodide perovskite solar cells. *Journal of Materials Chemistry A* **2015**, *3* (39), 19688-19695.
35. Kulbak, M.; Cahen, D.; Hodes, G., How Important Is the Organic Part of Lead Halide Perovskite Photovoltaic Cells? Efficient CsPbBr₃ Cells. *The Journal of Physical Chemistry Letters* **2015**, *6* (13), 2452-2456.
36. Burschka, J.; Pellet, N.; Moon, S.-J.; Humphry-Baker, R.; Gao, P.; Nazeeruddin, M. K.; Gratzel, M., Sequential deposition as a route to high-performance perovskite-sensitized solar cells. *Nature* **2013**, *499* (7458), 316-319.
37. Chen, H.-W.; Sakai, N.; Ikegami, M.; Miyasaka, T., Emergence of Hysteresis and Transient Ferroelectric Response in Organo-Lead Halide Perovskite Solar Cells. *The Journal of Physical Chemistry Letters* **2014**, *6* (1), 164-169.
38. Kim, H.-S.; Park, N.-G., Parameters Affecting I-V Hysteresis of CH₃NH₃PbI₃ Perovskite Solar Cells: Effects of Perovskite Crystal Size and Mesoporous TiO₂ Layer. *The Journal of Physical Chemistry Letters* **2014**, *5* (17), 2927-2934.
39. Meng, L.; You, J.; Guo, T.-F.; Yang, Y., Recent Advances in the Inverted Planar Structure of Perovskite Solar Cells. *Accounts of Chemical Research* **2016**, *49* (1), 155-165.
40. Im, J.-H.; Kim, H.-S.; Park, N.-G., Morphology-photovoltaic property correlation in perovskite solar cells: One-step versus two-step deposition of CH₃NH₃PbI₃. *APL Mater.* **2014**, *2* (8), 081510.
41. Jeon, N. J.; Noh, J. H.; Kim, Y. C.; Yang, W. S.; Ryu, S.; Seok, S. I., Solvent engineering for high-performance inorganic-organic hybrid perovskite solar cells. *Nat Mater* **2014**, *13* (9), 897-903.
42. Ahn, N.; Son, D.-Y.; Jang, I.-H.; Kang, S. M.; Choi, M.; Park, N.-G., Highly Reproducible Perovskite Solar Cells with Average Efficiency of 18.3% and Best Efficiency of 19.7% Fabricated via Lewis Base Adduct of Lead(II) Iodide. *Journal of the American Chemical Society* **2015**.
43. Xiao, M.; Huang, F.; Huang, W.; Dkhissi, Y.; Zhu, Y.; Etheridge, J.; Gray-Weale, A.; Bach, U.; Cheng, Y.-B.; Spiccia, L., A Fast Deposition-Crystallization Procedure for Highly Efficient Lead Iodide

Perovskite Thin-Film Solar Cells. *Angewandte Chemie* **2014**, *126* (37), 10056-10061.

44. Im, J.-H.; Jang, I.-H.; Pellet, N.; Grätzel, M.; Park, N.-G., Growth of $\text{CH}_3\text{NH}_3\text{PbI}_3$ cuboids with controlled size for high-efficiency perovskite solar cells. *Nat Nano* **2014**, *9* (11), 927-932.

45. Prasad, B. L. V.; Stoeva, S. I.; Sorensen, C. M.; Klabunde, K. J., Digestive Ripening of Thiolated Gold Nanoparticles: The Effect of Alkyl Chain Length. *Langmuir* **2002**, *18* (20), 7515-7520.

46. Lee, J.-S.; Shevchenko, E. V.; Talapin, D. V., Au–PbS Core–Shell Nanocrystals: Plasmonic Absorption Enhancement and Electrical Doping via Intra-particle Charge Transfer. *Journal of the American Chemical Society* **2008**, *130* (30), 9673-9675.

47. Achermann, M., Exciton–Plasmon Interactions in Metal–Semiconductor Nanostructures. *The Journal of Physical Chemistry Letters* **2010**, *1* (19), 2837-2843.

48. Kim, J.; Kim, G.; Kim, T. K.; Kwon, S.; Back, H.; Lee, J.; Lee, S. H.; Kang, H.; Lee, K., Efficient planar-heterojunction perovskite solar cells achieved via interfacial modification of a sol-gel ZnO electron collection layer. *Journal of Materials Chemistry A* **2014**, *2* (41), 17291-17296.

49. You, J.; Meng, L.; Song, T.-B.; Guo, T.-F.; Yang, Y.; Chang, W.-H.; Hong, Z.; Chen, H.; Zhou, H.; Chen, Q.; Liu, Y.; De Marco, N.; Yang, Y., Improved air stability of perovskite solar cells via solution-processed metal oxide transport layers. *Nat Nano* **2016**, *11* (1), 75-81.

50. Sutherland, B. R.; Hoogland, S.; Adachi, M. M.; Kanjanaboos, P.; Wong, C. T. O.; McDowell, J. J.; Xu, J.; Voznyy, O.; Ning, Z.; Houtepen, A. J.; Sargent, E. H., Perovskite Thin Films via Atomic Layer Deposition. *Advanced Materials* **2015**, *27* (1), 53-58.

51. Ko, H.-S.; Lee, J.-W.; Park, N.-G., 15.76% efficiency perovskite solar cells prepared under high relative humidity: importance of PbI_2 morphology in two-step deposition of $\text{CH}_3\text{NH}_3\text{PbI}_3$. *Journal of Materials Chemistry A* **2015**, *3* (16), 8808-8815.

52. Moreels, I.; Lambert, K.; Smeets, D.; De Muynck, D.; Nollet, T.; Martins, J. C.; Vanhaecke, F.; Vantomme, A.; Delerue, C.; Allan, G.; Hens, Z., Size-Dependent Optical Properties of Colloidal PbS Quantum Dots. *ACS Nano* **2009**, *3* (10), 3023-3030.

요 약 문

효율적인 페로브스카이트 태양 전지를 위한 정공 전달용 콜로이드 나노 입자 개발

본 연구는 용액 상태의 콜로이드 퀀텀 닷 나노 입자를 합성하여 페로브스카이트 태양 전지의 정공 전달 층에 적용시켜 보았다. 우선 hot-injection 방법으로 합성하였으며, PbS 퀀텀 닷의 특성인 사이즈별 밴드갭 조정과 높은 흡광 계수, 유기 전도성 물질 대비 낮은 가격의 특성을 가진 것을 바탕으로 n-i-p 접합 구조를 가진 다공성 페로브스카이트 층에 평균 3nm 사이즈의 나노 입자를 용액 공정 중 하나인 스프인코팅을 진행하였다. 밴드갭이 다른 PbS 물질을 적용시킨 소자는 정공 전달체가 없는 태양 전지에 비해 향상된 전류 밀도 (current density)를 가졌지만 개방전압(open circuit voltage)은 예상과 달리 감소했다. 개방 전압이 감소한 요인은 유기 리간드와 불완전한 계면으로 인한 것으로 보인다. 반면 전류 밀도는 PbS QDs에서 생성된 전하 및 페로브스카이트 층에서 생성된 정공 전달 향상과 연관되어 있는 것으로 예상된다. 최대 효율은 6.7%를 기록했다. 또한 au 나노입자의 plasmon과 PbS의 exciton의 관계로 강한 p타입 도핑 효과를 가지는 Au-PbS 코어셸 나노 입자를 합성해 페로브스카이트 정공 층에 적용시켜보았지만 효율은 PbS에 비해 감소했다.

값싼 구리를 기반으로 한 4원계 원소인 CZTS(구리, 아연, 주석, 황)와 CZTSe(구리, 아연, 주석, 셀레늄)를 hot-injection 방식으로 합성하여 정공 층에 적용해보았다. 그 결과 무정공층 페로브스카이 소자에 비해 향상된 전하밀도와 개방전압을 보여주었다. 향상된 전하밀도는 광에너지 전환 효율 증가 및 정공 전달 향상과 연관되며, 증가된 개방 전압은 낮은 valence band level의 위치와 페로브스카이 대비 높은 conduction band level로 인한 것임을 알 수 있었다. 태양전지의 최대 효율은 7.5%를 달성했다. 콜로이드 퀀텀 닷 나노입자를 페로브스카이트 태양전지의 정공 전달 층으로 적용해봄으로써 기존 유기물질 기반의 페로브스카이트 태양전지가 갖고 있는 가격 및 상용화 문제, 안정성 문제를 해소해줄 것으로 기대된다.